

# Synchrotron self-Compton in a radiative-adiabatic fireball scenario: Modelling the multiwavelength observations in some *Fermi*/LAT bursts

Nissim Fraija<sup>1</sup>,<sup>\*</sup> P. Veres<sup>2</sup>, B. Betancourt Kamenetskaia<sup>3,4</sup>, A. Galvan-Gamez<sup>1</sup>, M.G. Dainotti<sup>5,6,7,8</sup>,  
Simone Dichiara<sup>9</sup>, and R. L. Becerra<sup>10</sup>

<sup>1</sup>*Instituto de Astronomía, Universidad Nacional Autónoma de México, Circuito Exterior, C.U., A. Postal 70-264, 04510 Cd. de México, México.*

<sup>2</sup>*Center for Space Plasma and Aeronomic Research (CSPAR), University of Alabama in Huntsville, Huntsville, AL 35899, USA*

<sup>3</sup>*Technical University of Munich, TUM School of Natural Sciences, Physics Department, James-Frank-Str 1, 85748 Garching, Germany*

<sup>4</sup>*Max-Planck-Institut für Physik (Werner-Heisenberg-Institut), Föhringer Ring 6, 80805 Munich, Germany*

<sup>5</sup>*Division of Science, National Astronomical Observatory of Japan, 2-21-1 Osawa, Mitaka, Tokyo 181-8588, Japan*

<sup>6</sup>*The Graduate University for Advanced Studies (SOKENDAI), 2-21-1 Osawa, Mitaka, Tokyo 181-8588, Japan*

<sup>7</sup>*Space Science Institute, 4750 Walnut Street, Boulder, CO 80301, USA*

<sup>8</sup>*SLAC National Accelerator Laboratory, 2575 Sand Hill Road, Menlo Park, CA 94025, USA*

<sup>9</sup>*Department of Astronomy and Astrophysics, The Pennsylvania State University, 525 Davey Lab, University Park, PA 16802, USA*

<sup>10</sup>*Department of Physics, University of Rome - Tor Vergata, via della Ricerca Scientifica 1, 00100 Rome, IT*

Accepted XXX. Received YYY; in original form ZZZ

## ABSTRACT

Energetic GeV photons expected from the closest and the most energetic Gamma-ray bursts (GRBs) provide an unique opportunity to study the very-high-energy emission as well as the possible correlations with lower energy bands in realistic GRB afterglow models. In the standard GRB afterglow model, the relativistic homogeneous shock is usually considered to be fully adiabatic, however, it could be partially radiative. Based on the external forward-shock scenario in both stellar wind and constant-density medium. We present a radiative-adiabatic analytical model of the synchrotron self-Compton (SSC) and synchrotron processes considering an electron energy distribution with a power-law index of  $1 < p < 2$  and  $2 \leq p$ . We show that the SSC scenario plays a relevant role in the radiative parameter  $\epsilon$ , leading to a prolonged evolution during the slow cooling regime. In a particular case, we derive the *Fermi*/LAT light curves together with the photons with energies  $\geq 100$  MeV in a sample of nine bursts from the second *Fermi*/LAT GRB catalog that exhibited temporal and spectral indices with  $\gtrsim 1.5$  and  $\approx 2$ , respectively. These events can hardly be described with closure relations of the standard synchrotron afterglow model, and also exhibit energetic photons above the synchrotron limit. We have modeled the multi-wavelength observations of our sample to constrain the microphysical parameters, the circumburst density, the bulk Lorentz factor and the mechanism responsible for explaining the energetic GeV photons.

**Key words:** gamma-ray burst : General – Physical data and processes : acceleration of particles – Physical data and processes radiation mechanisms: non-thermal

## 1 INTRODUCTION

Gamma-ray bursts (GRBs) releasing  $\sim 10^{51} - 10^{55}$  erg of isotropic equivalent gamma-ray energy are the most energetic transient sources in the Universe. These transient events can last from a few milliseconds to several hours (Piran 1999; Kumar & Zhang 2015), and the duration of this prompt episode classifies GRBs into either short or long. The prompt emission is usually detected in the keV-MeV energy range (Kouveliotou et al. 1993) and is described by an empirical Band function (Band et al. 1993). The late and long-lasting emission, named “afterglow”, detected from radio to TeV gamma-rays, is usually interpreted within the fireball scenario (e.g. see Cavallo & Rees 1978). The fireball model predicts an external shock when a relativistic jet transfers a large part of its energy to the circumburst medium (Piran 1999). A fraction of the total energy is constantly transferred during the shock to accelerate electrons ( $\epsilon_e$ ) amplifying the magnetic field ( $\epsilon_B$ ). These electrons are cooled down mainly by synchrotron radiation emitting photons from radio to gamma-rays (Sari et al. 1998; Kumar & Barniol Duran 2009, 2010; Ackermann et al. 2013; Fraija et al. 2016a) and by very-high-energy (VHE  $\geq 100$  GeV) photons, which are radiated through the synchrotron self-Compton (SSC) mechanism (Fraija et al. 2019c,b; Zhang 2019).

In the standard GRB afterglow scenario, the relativistic forward shock (FS) is usually considered to be fully adiabatic, although it can be

\* E-mail: nifraija@astro.unam.mx

partially or fully radiative (Dai & Lu 1998; Sari et al. 1998; Böttcher & Dermer 2000; Ghisellini et al. 2010). The shock-accelerated electrons are in the fast-cooling regime when the dynamical timescale is larger than the cooling timescale. When accelerated electrons lie in the fast-cooling regime and also the microphysical parameter  $\epsilon_e$  is much greater than 0.1, the afterglow phase should be in the radiative regime instead of the adiabatic one (Böttcher & Dermer 2000; Li et al. 2002; Panaitescu 2019). Once the afterglow enters the slow-cooling regime, the hydrodynamic evolution can be approximated by the adiabatic case (e.g., see Moderski et al. 2000). The deceleration of the GRB fireball by the circumburst medium is faster when the fireball is radiative than when it is adiabatic. Therefore, the temporal afterglow evolution of synchrotron light curves and the shock energetics are modified (Böttcher & Dermer 2000; Wu et al. 2005). Ghisellini et al. (2010) studied the high-energy ( $> 100$  MeV) emission of 11 GRBs detected by the *Fermi*/LAT (Large Area Telescope) until 2009 October. They found that the temporal decay indices were consistent with synchrotron afterglow flux from a GRB fireball in the fully radiative regime. They proposed that a radiatively efficient fireball could explain the efficiency problem observed during the early afterglow (Zhang et al. 2007).

Ajello et al. (2019a) reported the second *Fermi*/LAT GRB catalog (2FLGC), covering 10 years (from 2008 to 2018) with a total of 169 bursts with high-energy photons above 100 MeV and 29 bursts above 10 GeV. In this sample, half of them (86/169) of LAT-detected bursts exhibited a temporally-extended component whereas 21/169 GRBs displayed a temporal break spanning from a few dozen to thousands of seconds. While the persistent emission is often attributed to standard synchrotron radiation originating from external FSs (Kumar & Barniol Duran 2009, 2010), it is worth noting that not all of the light curves detected by the LAT instrument adhere to the predicted closure relations between power-law (PL) temporal ( $\alpha_L$ ) and spectral ( $\Gamma_L$ ) indices (e.g., see Tak et al. 2019; Fraija et al. 2022a). This is the case of those GRBs that exhibit PL temporal and spectral indices of  $\alpha_L \gtrsim 1.5$  and  $\Gamma_L \approx 2$ , respectively.

Fraija et al. (2019b) derived the light curves and spectra of the SSC model for a wind and homogeneous medium for the adiabatic regime and an electron spectral index larger than 2 ( $2 < p$ ). The authors showed that the SSC framework could explain photons beyond the synchrotron limit in GRB 190114C. In this paper, we consider the deceleration phase of a relativistic outflow in a stellar wind and homogeneous medium and derive the expected light curves and spectra of the synchrotron and SSC FS model in the radiative regime for an electron spectral index in the range of  $1 < p < 2$  and  $2 \leq p$ . The closure relations of the synchrotron and the SSC FS model as a function of the radiative parameter ( $\epsilon$ ) are presented. We apply the proposed model to a representative sample of GRBs reported in the 2FLGC with values of temporal and spectral indices with  $\alpha_L \gtrsim 1.5$  and  $\Gamma_L \approx 2$ , which can hardly be described with closure relations of the standard (non-radiative) synchrotron afterglow model, and also exhibit energetic photons above the synchrotron limit (e.g., see Ghisellini et al. 2010; Tak et al. 2019; Fraija et al. 2022a). The paper is arranged as follows. Section 2 presents the SSC FS model as a function of the radiative parameter when the afterglow model evolves in a stellar wind and in a homogeneous medium. In Section 3, we apply our current model to a representative sample of GRBs reported in the 2FLGC and discuss the results, and finally, in Section 4, we summarise our results and present our conclusions. The convention  $Q_x = Q/10^x$  in cgs units and the universal constants  $c = \hbar = 1$  in natural units will be adopted throughout this paper.

## 2 SYNCHROTRON SELF-COMPTON AFTERGLOW MODEL

The long-lived afterglow emission is generated when a relativistic GRB outflow decelerates and drives a FS into the circumstellar medium. The outflow transfers a large amount of its energy to this surrounding external medium during the deceleration phase. Here, we extend the SSC afterglow model introduced in Fraija et al. (2019b), considering that the dynamics of the afterglow emission evolves in the radiative regime, and the electron distribution is described with a hard spectral index in the range of  $1 < p < 2$ . Additionally, we show the synchrotron light curves in the radiative regime for  $1 < p < 2$  and  $2 \leq p$ . We note that the self-absorption frequency does not affect the VHE emission.

### 2.1 Dynamics and afterglow emission in a stellar-wind medium

The dynamics of the afterglow emission for an outflow propagating into a stellar wind medium with a density profile  $\rho(r) \propto r^{-2}$  has been widely discussed in the particular case when it evolves in the adiabatic regime, and the electron distribution is described with  $2 < p$  (e.g., see Chevalier & Li 2000; Panaitescu & Mészáros 1998). Relativistic electrons are accelerated in the FS and efficiently cooled by synchrotron and SSC processes. In general, with the isotropic-equivalent kinetic energy<sup>1</sup>  $E_K = E \left( \frac{\Gamma}{\Gamma_0} \right)^\epsilon$  (Ghisellini et al. 2010; Fraija et al. 2023) and at a considerable distance from the progenitor  $R = 2 \Gamma^2 t / (1+z)$ , the evolution of the bulk Lorentz factor in the adiabatic and radiative regime considering the Blandford-McKee solution ( $E_K \propto (2 - \epsilon)\rho(r)r^3\Gamma^2$ ) (Blandford & McKee 1976) is  $\Gamma = 92.6 \left( \frac{1+z}{1.1} \right)^{\frac{1}{4-\epsilon}} A_{W,-1}^{-\frac{1}{4-\epsilon}} E_{53}^{\frac{1}{4-\epsilon}} \Gamma_{0,2}^{-\frac{\epsilon}{4-\epsilon}} t_{4.7}^{-\frac{1}{4-\epsilon}}$ . The term  $A_W$  is the parameter of wind density (Dai & Lu 1998; Chevalier & Li 2000; Vink & de Koter 2005), and  $\Gamma_0$  is the initial Lorentz factor. The parameter  $\epsilon$  takes into account the hydrodynamic evolution of the FS in the fully adiabatic ( $\epsilon = 0$ ), fully radiative ( $\epsilon = 1$ ) or partially radiative or adiabatic ( $0 < \epsilon < 1$ ) regimes (Böttcher & Dermer 2000; Wu et al. 2005; Ghisellini et al. 2010). The Lorentz factors of the lowest-energy electrons are  $\gamma_m = \left[ \tilde{g} \frac{m_p}{m_e} \epsilon_e \Gamma \gamma_M \right]^{\frac{1}{p-1}}$  with  $\tilde{g} = \frac{2-p}{p-1}$  for  $1 < p < 2$  and  $\gamma_m = g \frac{m_p}{m_e} \epsilon_e \Gamma$  for  $2 \leq p$ . In this last case,  $g = \ln \left( \frac{\gamma_M}{\gamma_m} \right)$  for  $p = 2$  and  $g = \frac{p-2}{p-1}$  for  $2 < p$  (Dai & Cheng 2001). The term  $\gamma_M$  corresponds to the maximum electron Lorentz factor, and  $m_p$  and  $m_e$  to the proton and electron mass, respectively. The Lorentz factor above which the electrons cool efficiently is  $\gamma_c = \frac{6\pi m_e c}{\sigma_T} (1+Y)^{-1} \Gamma^{-1} B'^{-2} t^{-1}$  where  $B'$  is the

<sup>1</sup> The isotropic gamma-ray energy  $E_{\gamma,\text{iso}}$  defines the isotropic-equivalent kinetic energy through kinetic efficiency  $\eta_K = E_{\gamma,\text{iso}} / (E_K + E_{\gamma,\text{iso}})$ .

comoving magnetic field in the blastwave,  $c$  is the speed of light,  $\sigma_T$  is the Thompson cross section and  $Y$  is the Compton parameter (e.g., see Fraija et al. 2023). When SSC emission becomes the dominant one in electron cooling (as compact radio sources; see Tsang & Kirk 2007), the electron population preferentially decreases the amount of energy available on  $U_{\text{SSC},1\text{st}}$  rather than  $U_{\text{syn}}$ , where  $U_{\text{syn}}$  and  $U_{\text{SSC},1\text{st}}$  are the energy density of synchrotron emission and the first-order scattering, respectively (e.g., see Kumar & Panaitescu 2008; Kobayashi et al. 2007; Petropoulou et al. 2015; Fraija & Veres 2018). In this case, it is needed to take into account the second-order Compton scatterings and therefore, the Lorentz factor above which the electrons cool efficiently is reduced by  $(1+Y+Y^2)$ , where the Compton parameter of second-order scattering is  $Y^2 \equiv \frac{U_{\text{IC},1\text{st}}}{U_{\text{B}}} = \frac{U_{\text{SSC},1\text{st}} U_{\text{syn}}}{U_{\text{syn}} U_{\text{B}}}$  with  $U_{\text{B}}$  the energy density of magnetic field (Kobayashi et al. 2007; Fraija & Veres 2018). It is worth noting that the Klein-Nishina (KN) effect allows us to ignore higher order (three or more) scattering. For a particular analysis and discussion of the range of parameter space considering this effect, see Petropoulou et al. (2015); Fraija & Veres (2018). We have adopted the unprimed and primed quantities to denote them in the observer and comoving frames, respectively. The Lorentz factors of the lowest-energy electrons and the Lorentz factor of the higher-energy electrons that cool efficiently by synchrotron process are given by

$$\gamma_m = \begin{cases} 4.9 \times 10^2 \tilde{g} \frac{1}{p-1} \left( \frac{1+z}{1.1} \right)^{\frac{8+p(\epsilon-3)-2\epsilon}{2(4-\epsilon)(p-1)}} \epsilon_{e,-1}^{\frac{1}{p-1}} \epsilon_{B,-4}^{\frac{-(p-2)}{4(p-1)}} A_{W,-1}^{\frac{8+p(\epsilon-6)-2\epsilon}{4(p-1)(4-\epsilon)}} E_{53}^{\frac{p}{2(p-1)(4-\epsilon)}} \Gamma_{0,2}^{-\frac{p\epsilon}{2(4-\epsilon)(p-1)}} t_{4.7}^{\frac{2\epsilon+p(3-\epsilon)-8}{2(4-\epsilon)(p-1)}} & \text{for } 1 < p < 2 \\ 1.6 \times 10^3 g \left( \frac{1+z}{1.1} \right)^{\frac{1}{4-\epsilon}} \epsilon_{e,-1} A_{W,-1}^{-\frac{1}{4-\epsilon}} E_{53}^{\frac{1}{4-\epsilon}} \Gamma_{0,2}^{-\frac{\epsilon}{4-\epsilon}} t_{4.7}^{-\frac{1}{4-\epsilon}} & \text{for } 2 \leq p \end{cases} \quad (1)$$

$$\gamma_c = 3.3 \times 10^3 (1+Y(\gamma_c))^{-1} \left( \frac{1+z}{1.1} \right)^{\frac{\epsilon-3}{4-\epsilon}} \epsilon_{B,-4} A_{W,-1}^{\frac{\epsilon-5}{4-\epsilon}} E_{53}^{\frac{1}{4-\epsilon}} \Gamma_{0,2}^{-\frac{\epsilon}{4-\epsilon}} t_{4.7}^{\frac{3-\epsilon}{4-\epsilon}}.$$

Hereafter, we use the spectral index  $p = 1.9$  ( $\tilde{g} \approx 0.1$ ) for  $1 < p < 2$  and  $p = 2.1$  ( $g \approx 0.09$ ) for  $2 < p$  to estimate the proportionality constant in each quantity. The terms  $\epsilon$  and the Compton parameter ( $Y$ ) are defined in subsections 2.3 and 2.4, respectively. The transition time from the fast- to the slow-cooling regime is (i.e., see Böttcher & Dermer 2000; Wu et al. 2005)

$$t_{\text{cm}} = \begin{cases} 8.4 \times 10^3 \text{ s } \tilde{g} \frac{2(4-\epsilon)}{S_1} \left( \frac{1+z}{1.1} \right) (1+Y(\gamma_c)) \frac{2(p-1)(4-\epsilon)}{S_1} \frac{2(4-\epsilon)}{S_1} \epsilon_{e,-1} \epsilon_{B,-4} \frac{(3p-2)(4-\epsilon)}{2S_1} A_{W,-1}^{\frac{14p-12+\epsilon(2-3p)}{2S_1}} E_{53}^{-\frac{p-2}{S_1}} \Gamma_{0,2}^{\frac{\epsilon(p-2)}{S_1}} & \text{for } 1 < p < 2 \\ 2.4 \times 10^4 \text{ s } g \left( \frac{1+z}{1.1} \right) (1+Y(\gamma_c)) \epsilon_{e,-1} \epsilon_{B,-4} A_{W,-1} & \text{for } 2 \leq p, \end{cases}$$

where  $S_1 = 3p + 2 - p\epsilon$ . Given the total number of emitting electrons ( $N_e$ ), and the synchrotron radiation power ( $P_\nu$ ; Panaitescu & Mészáros 1998; Sari et al. 1998; Chevalier & Li 2000), the spectral breaks ( $\nu_{\text{m,c}}^{\text{syn}} = \frac{q_e}{2\pi m_e c} (1+z)^{-1} \Gamma \gamma_{\text{m,c}}^2 B'$  with  $q_e$  the electron charge) and the maximum flux ( $F_{\text{max}}^{\text{syn}} = \frac{(1+z)^2}{4\pi D_z^2} N_e P_\nu$ ) in the synchrotron scenario can be written as

$$\nu_{\text{m}}^{\text{syn}} = \begin{cases} 4.2 \times 10^{11} \text{ Hz } \tilde{g} \frac{2}{p-1} \left( \frac{1+z}{1.1} \right)^{\frac{8-3p-2\epsilon+p\epsilon}{(4-\epsilon)(p-1)}} \epsilon_{e,-1}^{\frac{2}{p-1}} \epsilon_{B,-4}^{\frac{1}{2(p-1)}} A_{W,-1}^{\frac{4-2p-\epsilon}{2(p-1)(4-\epsilon)}} E_{53}^{\frac{p}{(p-1)(4-\epsilon)}} \Gamma_{0,2}^{-\frac{p\epsilon}{(4-\epsilon)(p-1)}} t_{4.7}^{\frac{\epsilon-p-4}{(4-\epsilon)(p-1)}} & \text{for } 1 < p < 2 \\ 4.2 \times 10^{12} \text{ Hz } g^2 \left( \frac{1+z}{1.1} \right)^{\frac{2}{4-\epsilon}} \epsilon_{B,-4}^{\frac{1}{2}} \epsilon_{e,-1}^2 A_{W,-1}^{-\frac{\epsilon}{2(4-\epsilon)}} E_{53}^{\frac{2}{4-\epsilon}} \Gamma_{0,2}^{-\frac{2\epsilon}{4-\epsilon}} t_{4.7}^{\frac{\epsilon-6}{4-\epsilon}} & \text{for } 2 \leq p \end{cases}$$

$$\nu_c^{\text{syn}} = 6.8 \times 10^{12} \text{ Hz } (1+Y(\gamma_c))^{-2} \left( \frac{1+z}{1.1} \right)^{\frac{2(\epsilon-3)}{4-\epsilon}} \epsilon_{B,-4}^{-\frac{3}{2}} A_{W,-1}^{\frac{3\epsilon-16}{2(4-\epsilon)}} E_{53}^{\frac{2}{4-\epsilon}} \Gamma_{0,2}^{-\frac{2\epsilon}{4-\epsilon}} t_{4.7}^{\frac{2-\epsilon}{4-\epsilon}}$$

$$F_{\text{max}}^{\text{syn}} = 9.1 \times 10^3 \text{ mJy } \left( \frac{1+z}{1.1} \right)^{\frac{2(5-\epsilon)}{4-\epsilon}} \epsilon_{B,-4}^{\frac{1}{2}} D_{z,27}^{-2} A_{W,-1}^{\frac{8-3\epsilon}{2(4-\epsilon)}} E_{53}^{\frac{2}{4-\epsilon}} \Gamma_{0,2}^{-\frac{2\epsilon}{4-\epsilon}} t_{4.7}^{-\frac{2}{4-\epsilon}},$$

where the term  $D_z$  corresponds to the luminosity distance, which is estimated using the cosmological parameters reported in Planck Collaboration et al. (2018). Given the maximum Lorentz factor of the electron distribution  $\gamma_{\text{max}} = \left( \frac{3q_e}{\xi \sigma_T} B'^{-1} \right)^{\frac{1}{2}}$  with  $\xi$  the Bohm parameter<sup>2</sup> (Piran & Nakar 2010), the evolution of the maximum energy photon radiated by the synchrotron process in the stellar-wind medium ( $h\nu_{\text{max}}^{\text{syn}} = \frac{3q_e^2}{2\pi \sigma_T m_e c} (1+z)^{-1} \Gamma$ ) can be written as (Fraija et al. 2024)

$$h\nu_{\text{max}}^{\text{syn}} = 0.6 \text{ GeV } \left( \frac{1+z}{1.1} \right)^{\frac{\epsilon-3}{4-\epsilon}} A_{W,-1}^{-\frac{1}{4-\epsilon}} E_{53}^{\frac{1}{4-\epsilon}} \Gamma_{0,2}^{-\frac{\epsilon}{4-\epsilon}} t_{4.7}^{-\frac{1}{4-\epsilon}}. \quad (2)$$

Using Eqs. (2.1) and the synchrotron spectra for the fast- and slow-cooling regimes (Sari et al. 1998), we find that the synchrotron light curves at an observed frequency  $\nu$  and a given time  $t$  for  $1 < p < 2$  and  $2 \leq p$  evolve as

$$F_\nu^{\text{syn}} \propto \begin{cases} (1 < p < 2) & (2 \leq p) \\ \left\{ t^{\frac{\epsilon-8}{3(4-\epsilon)}}, t^{-\frac{5p+\epsilon-10}{3(p-1)(4-\epsilon)}} \right\} \nu^{\frac{1}{3}} & \left\{ t^{\frac{\epsilon-8}{3(4-\epsilon)}}, t^{-\frac{\epsilon}{3(4-\epsilon)}} \right\} \nu^{\frac{1}{3}}, & \text{for } \nu < \{\nu_c^{\text{syn}}, \nu_m^{\text{syn}}\}, \\ t^{-\frac{\epsilon+2}{2(4-\epsilon)}} \nu^{-\frac{1}{2}}, & t^{-\frac{\epsilon+2}{2(4-\epsilon)}} \nu^{-\frac{1}{2}} & \text{for } \nu_c^{\text{syn}} < \nu < \nu_m^{\text{syn}}, \\ t^{\frac{\epsilon-p-8}{2(4-\epsilon)}} \nu^{-\frac{p-1}{2}}, & t^{\frac{2-6p-\epsilon+p\epsilon}{2(4-\epsilon)}} \nu^{-\frac{p-1}{2}} & \text{for } \nu_m^{\text{syn}} < \nu < \nu_c^{\text{syn}}, \\ t^{-\frac{p+6}{2(4-\epsilon)}} \nu^{-\frac{p}{2}} & t^{\frac{4+p(\epsilon-6)-2\epsilon}{2(4-\epsilon)}} \nu^{-\frac{p}{2}}, & \text{for } \{\nu_m^{\text{syn}}, \nu_c^{\text{syn}}\} < \nu. \end{cases}$$

In order to show the evolution of the rest of parameters as a function of  $\epsilon$ , e.g. for  $\{\nu_m^{\text{syn}}, \nu_c^{\text{syn}}\} < \nu$  the synchrotron flux yields

<sup>2</sup> The value of this parameter becomes  $\xi \sim 1$  in the Bohm limit.

$$F_{1 < p < 2}^{\text{syn}} \propto g(p)(1+z)^{\frac{22+p(\epsilon-3)-4\epsilon}{2(4-\epsilon)}} (1+Y(\gamma_c))^{-1} A_W^{\frac{2(1-\epsilon)-p}{2(4-\epsilon)}} D_z^{-2} \epsilon_e E^{\frac{p+6}{2(4-\epsilon)}} \Gamma_0^{-\frac{\epsilon(p+6)}{2(4-\epsilon)}},$$

$$F_{2 \leq p}^{\text{syn}} \propto g(p)p^{-1}(1+z)^{\frac{6+p-\epsilon}{4-\epsilon}} (1+Y(\gamma_c))^{-1} A_W^{-\frac{\epsilon(p+2)}{4(4-\epsilon)}} D_z^{-2} \epsilon_B^{\frac{p-2}{4}} \epsilon_e^{p-1} E^{\frac{p+2}{4-\epsilon}} \Gamma_0^{-\frac{\epsilon(p+2)}{4-\epsilon}}.$$

It is worth noting that for  $p \approx 2$ , synchrotron fluxes for  $1 < p < 2$  and  $2 \leq p$  are equal (i.e.,  $F_{1 < p < 2}^{\text{syn}} \approx F_{2 \leq p}^{\text{syn}}$ ).

The SSC process occurs when the same electron population that radiates synchrotron photons up-scatters them to higher energies as  $h\nu_k^{\text{SSC}} \sim \gamma_k^2 h\nu_k^{\text{syn}}$ . Here, the notation  $k = m, c$  refers to the minimum and cooling frequencies and  $h$  stands for the Planck constant (e.g., see [Sari & Esin 2001](#)). The maximum flux that the SSC process can reach  $F_{\text{max}}^{\text{SSC}} \sim \tau F_{\text{max}}^{\text{syn}}$  depends on the maximum synchrotron flux given in Eqs. (2.1) and the optical depth  $\tau \propto \frac{1}{3} A_W R^{-1}$ . Therefore, the spectral breaks and the maximum flux in the SSC scenario for  $1 < p < 2$  and  $2 \leq p$  are (e.g., see [Fraija et al. 2019b, 2022a](#))

$$h\nu_m^{\text{SSC}} = \begin{cases} 4.2 \times 10^2 \text{ eV } \bar{g}^{\frac{4}{p-1}} \left(\frac{1+z}{1.1}\right)^{\frac{2[8+p(\epsilon-3)-2\epsilon]}{(4-\epsilon)(p-1)}} \epsilon_{e,-1}^{\frac{p-1}{2}} \epsilon_{B,-4}^{\frac{3-p}{2(p-1)}} A_{W,-1}^{\frac{p(\epsilon-8)+3(4-\epsilon)}{2(p-1)(4-\epsilon)}} E_{53}^{\frac{2p}{(p-1)(4-\epsilon)}} \Gamma_{0,2}^{-\frac{2p\epsilon}{(4-\epsilon)(p-1)}} t_{4.7}^{\frac{3(\epsilon-4)-p(\epsilon-2)}{(4-\epsilon)(p-1)}} & \text{for } 1 < p < 2 \\ 4.1 \times 10^4 \text{ eV } g^4 \left(\frac{1+z}{1.1}\right)^{\frac{4}{4-\epsilon}} \epsilon_{B,-4}^{\frac{1}{2}} \epsilon_{e,-1}^4 A_{W,-1}^{-\frac{4+\epsilon}{2(4-\epsilon)}} E_{53}^{\frac{4}{4-\epsilon}} \Gamma_{0,2}^{-\frac{4\epsilon}{4-\epsilon}} t_{4.7}^{\frac{\epsilon-8}{4-\epsilon}} & \text{for } 2 \leq p \end{cases}$$

$$h\nu_c^{\text{SSC}} = 8.57 \times 10^{-3} \text{ GeV } (1+Y(\gamma_c))^{-4} \left(\frac{1+z}{1.1}\right)^{\frac{4(\epsilon-3)}{4-\epsilon}} \epsilon_{B,-4}^{-\frac{7}{2}} A_{W,-1}^{\frac{7\epsilon-36}{2(4-\epsilon)}} E_{53}^{\frac{4}{4-\epsilon}} \Gamma_{0,2}^{-\frac{4\epsilon}{4-\epsilon}} t_{4.7}^{\frac{8-3\epsilon}{4-\epsilon}}$$

$$F_{\text{max}}^{\text{SSC}} = 4.6 \times 10^{-5} \text{ mJy } g^{-1} \left(\frac{1+z}{1.1}\right)^3 \epsilon_{B,-4}^{\frac{1}{2}} D_{z,27}^{-2} A_{W,-1}^{\frac{5}{2}} t_{4.7}^{-1}.$$

Given the evolution of the spectral breaks and the maximum flux (Eqs. 3), it is possible to write the SSC light curves at an observed frequency  $\nu$  and a given time  $t$  as (e.g., see [Fraija et al. 2019b, 2022a](#))

$$F_{\nu}^{\text{SSC}} \propto \begin{cases} \begin{cases} (1 < p < 2) \\ \left\{ t^{\frac{2(3\epsilon-10)}{3(4-\epsilon)}, t^{\frac{2[12-7p+\epsilon(2p-3)]}{3(p-1)(4-\epsilon)}} \right\} \nu^{\frac{1}{3}}, & \begin{cases} (2 \leq p) \\ \left\{ t^{\frac{2(3\epsilon-10)}{3(4-\epsilon)}, t^{\frac{2(\epsilon-2)}{3(4-\epsilon)}} \right\} \nu^{\frac{1}{3}}, \end{cases} & \text{for } \nu < \{\nu_c^{\text{SSC}}, \nu_m^{\text{SSC}}\}, \\ t^{-\frac{\epsilon}{2(4-\epsilon)}} \nu^{-\frac{1}{2}}, & t^{-\frac{\epsilon}{2(4-\epsilon)}} \nu^{-\frac{1}{2}} & \text{for } \nu_c^{\text{SSC}} < \nu < \nu_m^{\text{SSC}}, \\ t^{\frac{2p+5\epsilon-20-p\epsilon}{2(4-\epsilon)}} \nu^{-\frac{p-1}{2}}, & t^{\frac{p(\epsilon-8)+\epsilon}{2(4-\epsilon)}} \nu^{-\frac{p-1}{2}} & \text{for } \nu_m^{\text{SSC}} < \nu < \nu_c^{\text{SSC}}, \\ t^{\frac{2(\epsilon-6)-p(\epsilon-2)}{2(4-\epsilon)}} \nu^{-\frac{p}{2}}, & t^{\frac{8+p(\epsilon-8)-2\epsilon}{2(4-\epsilon)}} \nu^{-\frac{p}{2}} & \text{for } \{\nu_m^{\text{SSC}}, \nu_c^{\text{SSC}}\} < \nu. \end{cases} \end{cases} \quad (4)$$

In order to show the evolution of the rest of parameters as a function of  $\epsilon$ , e.g. for  $\{\nu_m^{\text{SSC}}, \nu_c^{\text{SSC}}\} < \nu$ , the SSC flux yields

$$F_{1 < p < 2}^{\text{SSC}} \propto g(p)(1+z)^{\frac{14+p(\epsilon-3)+3\epsilon}{4-\epsilon}} (1+Y(\gamma_c))^{-2} A_W^{\frac{8(2-p)+\epsilon(p-6)}{4(4-\epsilon)}} D_z^{-2} \epsilon_B^{-\frac{p+2}{4}} \epsilon_e^2 E^{\frac{p+2}{4-\epsilon}} \Gamma_0^{-\frac{(p+2)\epsilon}{4-\epsilon}}$$

$$F_{2 \leq p}^{\text{SSC}} \propto g(p)^{2p-3} (1+z)^{\frac{4+2p-\epsilon}{4-\epsilon}} (1+Y(\gamma_c))^{-2} A_W^{\frac{4(2-p)-\epsilon(p+2)}{4(4-\epsilon)}} D_z^{-2} \epsilon_B^{\frac{p-6}{4}} \epsilon_e^{2(p-1)} E^{\frac{2p}{4-\epsilon}} \Gamma_0^{-\frac{2\epsilon p}{4-\epsilon}}.$$

We can see that SSC fluxes for  $1 < p < 2$  and  $2 \leq p$  are equal (i.e.,  $F_{1 < p < 2}^{\text{SSC}} \approx F_{2 \leq p}^{\text{SSC}}$ ) when  $p \approx 2$ .

It is worth noting that very energetic photons of energy  $h\nu_h \approx 1 \text{ TeV}$  interacting with low-energy photons  $h\nu_l = 60.1 \text{ eV} \left(\frac{\Gamma_l}{1+z}\right)^2 \frac{1}{(h\nu_h/1 \text{ TeV})}$  are absorbed to produce pairs (e.g., see [Fraija et al. 2019c](#)). The optical depth of attenuation of this interaction process is  $\tau_{\gamma\gamma} = 1.8 \times 10^{-8} \frac{R_{17}}{\Gamma_l} n_{\gamma,5.3}$ , where  $n_{\gamma} \approx 2.4 \times 10^3 \text{ cm}^{-3} \frac{L_{\gamma,44}}{R_{17}^2 \Gamma_l (h\nu_l/60.1 \text{ eV})}$  and  $L_{\gamma,44}$  are the photon density and luminosity of the seed photons, respectively (e.g., see [Piran 1999](#)).

## 2.2 Dynamics and afterglow emission in a uniform-density medium

Once the outflow begins to be decelerated at a significant distance from the progenitor by a uniform-density medium ( $\rho = n$ ), the evolution of the bulk Lorentz factor in the adiabatic and radiative regimes considering the Blandford-McKee solution ( $E_K = \frac{2\pi}{3} (2 - \epsilon) m_p c^2 n r^3 \Gamma^2$ ) ([Blandford & McKee 1976](#)) becomes  $\Gamma = 17.0 \left(\frac{1+z}{1.1}\right)^{\frac{3}{8-\epsilon}} n^{-\frac{1}{8-\epsilon}} E_{53}^{\frac{1}{8-\epsilon}} \Gamma_{0,2}^{-\frac{\epsilon}{8-\epsilon}} t_{4.7}^{-\frac{3}{8-\epsilon}}$  ([Ghisellini et al. 2010; Fraija et al. 2023](#)). In the case of a uniform-density medium, the Lorentz factors of both, the lowest-energy electrons and higher-energy electrons that cool efficiently by synchrotron process evolve as (i.e., see [Dai & Cheng 2001; Sari et al. 1998; Fraija et al. 2023](#))

$$\gamma_m = \begin{cases} 9.3 \times 10^2 \bar{g}^{\frac{1}{p-1}} \left(\frac{1+z}{1.1}\right)^{\frac{3(4-p)}{2(8-\epsilon)(p-1)}} \epsilon_{e,-1}^{\frac{1}{p-1}} \epsilon_{B,-4}^{\frac{-(p-2)}{4(p-1)}} n^{\frac{8-6p+p\epsilon-2\epsilon}{4(p-1)(8-\epsilon)}} E_{53}^{\frac{4-p}{2(p-1)(8-\epsilon)}} \Gamma_{0,2}^{-\frac{\epsilon(4-p)}{2(8-\epsilon)(p-1)}} t_{4.7}^{-\frac{3(4-p)}{2(8-\epsilon)(p-1)}} & \text{for } 1 < p < 2 \\ 3.4 \times 10^2 g \left(\frac{1+z}{1.1}\right)^{\frac{3}{8-\epsilon}} \epsilon_{e,-1} n^{-\frac{1}{8-\epsilon}} E_{53}^{\frac{1}{8-\epsilon}} \Gamma_{0,2}^{-\frac{\epsilon}{8-\epsilon}} t_{4.7}^{-\frac{3}{8-\epsilon}} & \text{for } 2 \leq p \end{cases} \quad (5)$$

$$\gamma_c = 1.6 \times 10^3 (1+Y(\gamma_c))^{-1} \left(\frac{1+z}{1.1}\right)^{-\frac{1+\epsilon}{8-\epsilon}} \epsilon_{B,-4}^{-1} n^{\frac{\epsilon-5}{8-\epsilon}} E_{53}^{-\frac{3}{8-\epsilon}} \Gamma_{0,2}^{\frac{3\epsilon}{8-\epsilon}} t_{4.7}^{\frac{1+\epsilon}{8-\epsilon}}. \quad (6)$$

The terms  $\epsilon$  and  $Y$  are defined in subsections 2.4 and 2.3, respectively. In this afterglow model, the transition time from the fast- to the slow-cooling regime takes place at (i.e., see Böttcher & Dermer 2000; Wu et al. 2005)

$$t_{\text{cm}} = \begin{cases} 4.8 \times 10^2 \text{ s } \tilde{g}^{\frac{2(8-\epsilon)}{S_2}} \left(\frac{1+z}{1.1}\right) (1+Y(\gamma_c)) \frac{2(p-1)(8-\epsilon)}{S_2} \frac{2(8-\epsilon)}{S_2} \frac{(3p-2)(8-\epsilon)}{2S_2} n^{\frac{14p-12+\epsilon(2-3p)}{2S_2}} E_{53}^{\frac{5p-2}{S_2}} \Gamma_{0,2}^{\frac{\epsilon(2-5p)}{S_2}} & \text{for } 1 < p < 2 \\ 3.0 \times 10^3 \text{ s } g^{\frac{8-\epsilon}{4+\epsilon}} \left(\frac{1+z}{1.1}\right) (1+Y(\gamma_c)) \frac{8-\epsilon}{4+\epsilon} \epsilon_{e,-1}^{\frac{8-\epsilon}{4+\epsilon}} \epsilon_{B,-4}^{\frac{8-\epsilon}{4+\epsilon}} n^{\frac{4-\epsilon}{4+\epsilon}} E_{53}^{\frac{4}{4+\epsilon}} \Gamma_{0,2}^{\frac{4\epsilon}{4+\epsilon}} & \text{for } 2 \leq p, \end{cases}$$

where  $S_2 = 10 - p + 2\epsilon(p-1)$ . In this case, given the electron Lorentz factors (Eq. 5), the synchrotron spectral breaks ( $\nu_{\text{m,c}}^{\text{syn}} \propto (1+z)^{-1} \Gamma \gamma_{\text{m,c}}^2 B'$ ) and the maximum flux ( $F_{\text{max}}^{\text{syn}} \propto (1+z)^2 D_z^{-2} N_e P_V$ ) become

$$\nu_{\text{m}}^{\text{syn}} = \begin{cases} 9.1 \times 10^9 \text{ Hz } \tilde{g}^{\frac{2}{p-1}} \left(\frac{1+z}{1.1}\right) \frac{14-5p+\epsilon(p-1)}{(8-\epsilon)(p-1)} \frac{2}{\epsilon_{e,-1}^{p-1}} \frac{1}{\epsilon_{B,-4}^{2(p-1)}} n^{\frac{4-2p-\epsilon}{2(p-1)(8-\epsilon)}} E_{53}^{\frac{p+2}{(p-1)(8-\epsilon)}} \Gamma_{0,2}^{-\frac{\epsilon(p+2)}{(8-\epsilon)(p-1)}} t_{4,7}^{-\frac{3(p+2)}{(8-\epsilon)(p-1)}} & \text{for } 1 < p < 2 \\ 3.5 \times 10^{11} \text{ Hz } g^2 \left(\frac{1+z}{1.1}\right) \frac{4+\epsilon}{8-\epsilon} \epsilon_{e,-1}^{\frac{4+\epsilon}{8-\epsilon}} \epsilon_{B,-4}^{\frac{1}{2}} n^{-\frac{\epsilon}{2(8-\epsilon)}} E_{53}^{\frac{4}{8-\epsilon}} \Gamma_{0,2}^{-\frac{4\epsilon}{8-\epsilon}} t_{4,7}^{-\frac{12}{8-\epsilon}} & \text{for } 2 \leq p \end{cases}$$

$$\nu_{\text{c}}^{\text{syn}} = 2.2 \times 10^{12} \text{ Hz } (1+Y(\gamma_c))^{-2} \left(\frac{1+z}{1.1}\right)^{-\frac{(4+\epsilon)}{8-\epsilon}} \epsilon_{B,-4}^{-\frac{3}{2}} n^{\frac{3\epsilon-16}{2(8-\epsilon)}} E_{53}^{-\frac{4}{8-\epsilon}} \Gamma_{0,2}^{\frac{4\epsilon}{8-\epsilon}} t_{4,7}^{\frac{2(\epsilon-2)}{8-\epsilon}}$$

$$F_{\text{max}}^{\text{syn}} = 8.1 \times 10 \text{ mJy } \left(\frac{1+z}{1.1}\right)^{\frac{\epsilon+16}{8-\epsilon}} \epsilon_{B,-4}^{\frac{1}{2}} D_{z,27}^{-2} n^{\frac{8-3\epsilon}{2(8-\epsilon)}} E_{53}^{\frac{8}{8-\epsilon}} \Gamma_{0,2}^{-\frac{8\epsilon}{8-\epsilon}} t_{4,7}^{-\frac{3\epsilon}{8-\epsilon}}.$$

The evolution of the maximum energy photon radiated by the synchrotron process in a homogeneous medium ( $h\nu_{\text{max}}^{\text{syn}} \propto (1+z)^{-1} \Gamma$ ) can be written as (Fraija et al. 2024)

$$h\nu_{\text{max}}^{\text{syn}} = 0.2 \text{ GeV } \left(\frac{1+z}{1.1}\right)^{\frac{\epsilon-5}{8-\epsilon}} n^{-\frac{1}{8-\epsilon}} E_{53}^{\frac{1}{8-\epsilon}} \Gamma_{0,2}^{-\frac{\epsilon}{8-\epsilon}} t_{4,7}^{-\frac{3}{8-\epsilon}}. \quad (8)$$

Using Eqs. 7, the synchrotron light curves at a specific time  $t$  and frequency  $\nu$  for  $1 < p < 2$  and  $2 \leq p$  can be written as (i.e., see Böttcher & Dermer 2000; Wu et al. 2005)

$$F_{\nu}^{\text{syn}} \propto \begin{cases} (1 < p < 2) & (2 \leq p) \\ \left\{ t^{\frac{4-11\epsilon}{3(8-\epsilon)}}, t^{\frac{(p+2)-3\epsilon(p-1)}{(8-\epsilon)(p-1)}} \right\} \nu^{\frac{1}{3}}, & \left\{ t^{\frac{4-11\epsilon}{3(8-\epsilon)}}, t^{\frac{4-3\epsilon}{8-\epsilon}} \right\} \nu^{\frac{1}{3}} & \text{for } \nu < \{\nu_{\text{c}}^{\text{syn}}, \nu_{\text{m}}^{\text{syn}}\}, \\ t^{-\frac{2(\epsilon+1)}{8-\epsilon}} \nu^{-\frac{1}{2}}, & t^{-\frac{2(\epsilon+1)}{8-\epsilon}} \nu^{-\frac{1}{2}} & \text{for } \nu_{\text{c}}^{\text{syn}} < \nu < \nu_{\text{m}}^{\text{syn}}, \\ t^{-\frac{3(p+2+2\epsilon)}{2(8-\epsilon)}} \nu^{-\frac{p-1}{2}}, & t^{-\frac{3(2-2p-\epsilon)}{8-\epsilon}} \nu^{-\frac{p-1}{2}}, & \text{for } \nu_{\text{m}}^{\text{syn}} < \nu < \nu_{\text{c}}^{\text{syn}}, \\ t^{-\frac{3p+10+4\epsilon}{2(8-\epsilon)}} \nu^{-\frac{p}{2}}, & t^{-\frac{2(2-3p-\epsilon)}{8-\epsilon}} \nu^{-\frac{p}{2}} & \text{for } \{\nu_{\text{m}}^{\text{syn}}, \nu_{\text{c}}^{\text{syn}}\} < \nu. \end{cases} \quad (9)$$

Given the electron Lorentz factors (Eqs. 5), the spectral breaks and the maximum flux of the synchrotron process (Eqs. 7) with the optical depth given by  $\tau \propto nR$ , the spectral breaks and the maximum flux in the SSC scenario for  $1 < p < 2$  and  $2 \leq p$  are (e.g., see Fraija et al. 2019b, 2022a)

$$h\nu_{\text{m}}^{\text{SSC}} = \begin{cases} 0.3 \text{ eV } \tilde{g}^{\frac{4}{p-1}} \left(\frac{1+z}{1.1}\right) \frac{26+p(\epsilon-8)-\epsilon}{(8-\epsilon)(p-1)} \frac{4}{\epsilon_{e,-1}^{p-1}} \epsilon_{B,-4}^{\frac{3-p}{2(p-1)}} n^{\frac{p(\epsilon-8)-3(\epsilon-4)}{2(p-1)(8-\epsilon)}} E_{53}^{\frac{6}{(p-1)(8-\epsilon)}} \Gamma_{0,2}^{-\frac{6\epsilon}{(8-\epsilon)(p-1)}} t_{4,7}^{-\frac{18}{(8-\epsilon)(p-1)}} & \text{for } 1 < p < 2 \\ 1.7 \times 10^2 \text{ eV } g^4 \left(\frac{1+z}{1.1}\right) \frac{10+\epsilon}{8-\epsilon} \epsilon_{e,-1}^4 \epsilon_{B,-4}^{\frac{1}{2}} n^{-\frac{4+\epsilon}{2(8-\epsilon)}} E_{53}^{\frac{6}{8-\epsilon}} \Gamma_{0,2}^{-\frac{6\epsilon}{8-\epsilon}} t_{4,7}^{-\frac{18}{8-\epsilon}} & \text{for } 2 \leq p \end{cases}$$

$$h\nu_{\text{c}}^{\text{SSC}} = 2.2 \times 10^{-5} \text{ GeV } \left(\frac{1+z}{1.1}\right)^{-\frac{3(\epsilon+2)}{8-\epsilon}} (1+Y(\gamma_c))^{-4} \epsilon_{B,-4}^{-\frac{7}{2}} n^{\frac{7\epsilon-36}{2(8-\epsilon)}} E_{53}^{-\frac{10}{8-\epsilon}} \Gamma_{0,2}^{\frac{10\epsilon}{8-\epsilon}} t_{4,7}^{\frac{2(2\epsilon-1)}{8-\epsilon}}$$

$$F_{\text{max}}^{\text{SSC}} = 3.9 \times 10^{-5} \text{ mJy } g^{-1} \left(\frac{1+z}{1.1}\right)^{\frac{2(\epsilon+7)}{8-\epsilon}} \epsilon_{B,-4}^{\frac{1}{2}} D_{z,27}^{-2} n^{\frac{5(4-\epsilon)}{2(8-\epsilon)}} E_{53}^{\frac{10}{8-\epsilon}} \Gamma_{0,2}^{-\frac{10\epsilon}{8-\epsilon}} t_{4,7}^{\frac{2(1-2\epsilon)}{8-\epsilon}},$$

respectively. Given the evolution of the spectral breaks and the maximum flux (Eqs. 10), it is possible to write the SSC light curves at an observed frequency  $\nu$  and a given time  $t$  for  $1 < p < 2$  and  $2 \leq p$  as (e.g., see Fraija et al. 2019b, 2022a)

$$F_{\nu}^{\text{SSC}} \propto \begin{cases} (1 < p < 2) & (2 \leq p) \\ \left\{ t^{\frac{8(1-2\epsilon)}{3(8-\epsilon)}}, t^{\frac{2(p+2)-4\epsilon(p-1)}{(8-\epsilon)(p-1)}} \right\} \nu^{\frac{1}{3}}, & \left\{ t^{\frac{8(1-2\epsilon)}{3(8-\epsilon)}}, t^{\frac{4(2-\epsilon)}{8-\epsilon}} \right\} \nu^{\frac{1}{3}} & \text{for } \nu < \{\nu_{\text{c}}^{\text{SSC}}, \nu_{\text{m}}^{\text{SSC}}\}, \\ t^{-\frac{1-2\epsilon}{8-\epsilon}} \nu^{-\frac{1}{2}}, & t^{-\frac{1-2\epsilon}{8-\epsilon}} \nu^{-\frac{1}{2}} & \text{for } \nu_{\text{c}}^{\text{SSC}} < \nu < \nu_{\text{m}}^{\text{SSC}}, \\ t^{-\frac{7+4\epsilon}{8-\epsilon}} \nu^{-\frac{p-1}{2}}, & t^{-\frac{11-4\epsilon-9p}{8-\epsilon}} \nu^{-\frac{p-1}{2}} & \text{for } \nu_{\text{m}}^{\text{SSC}} < \nu < \nu_{\text{c}}^{\text{SSC}}, \\ t^{-\frac{2(4+\epsilon)}{8-\epsilon}} \nu^{-\frac{p}{2}}, & t^{-\frac{10-2\epsilon-9p}{8-\epsilon}} \nu^{-\frac{p}{2}} & \text{for } \{\nu_{\text{m}}^{\text{SSC}}, \nu_{\text{c}}^{\text{SSC}}\} < \nu, \end{cases} \quad (11)$$

respectively. As discussed in the case of the stellar wind medium, VHE photons  $\sim 1$  TeV could be attenuated by interactions with softer photons.

### 2.3 Evolution of the radiative parameter

The radiative parameter is defined by the ratio between the radiated and dissipated energy (Nappo et al. 2014; Moderski et al. 2000). When the radiated and dissipated energies are similar almost most of the internal energy is dissipated as radiation, and the afterglow phase lies in the radiative regime. This parameter is defined as

$$\epsilon \equiv \epsilon_e \zeta, \quad (12)$$

where  $\zeta$  is the fraction of the radiated energy. It is estimated as the ratio of the power radiated during the slow- and fast-cooling regimes (Nappo et al. 2014)

$$\zeta = \begin{cases} \frac{\gamma_m^{p-2}}{\gamma_c^{p-2}} \left[ \frac{1}{p-2} \left( \frac{\gamma_c}{\gamma_m} \right)^{3-p} - 1 \right] & \text{for } \gamma_m \leq \gamma_c \\ 1 & \text{for } \gamma_c < \gamma_m. \end{cases} \quad (13)$$

Eqs. 12 and 13 show that the radiative parameter is constant  $\epsilon = \epsilon_e$  during the fast cooling regime. Afterwards it is expected to decrease to 0 during the slow cooling regime for  $2 \leq p$ . We notice that the radiative parameter decreases slowly if the value of  $p$  does not deviate from 2, and in the particular case when  $p \rightarrow 2$ , the radiative parameter approaches the same value  $\epsilon \simeq \epsilon_e$ . At the previous point, an adiabatic break was not observed. On the other hand, if  $p$  largely deviates from 2, adiabatic breaks around the transition time are expected in the synchrotron and SSC light curves. Eqs. 12 and 13 shows that the radiative parameter evolves during GRB.

**2.3.0.1 Equivalence with the radiative parameter  $s$ .** Some authors have introduced the radiative parameter  $s$  instead of  $\epsilon$  through the variation explicitly of the equivalent kinetic energy as (Böttcher & Dermer 2000; Wu et al. 2005; Ghisellini et al. 2010)

$$E \left( \frac{t}{t_{\text{dec}}} \right)^{-s} \propto (2 - \epsilon) \rho(r) \Gamma^2 R^{3-k}, \quad (14)$$

where  $\rho(r) \propto r^{-k}$  with  $k = 0$  corresponds to the density of the constant-density medium ( $\rho = n$ ), and  $k = 2$  to the density of the stellar wind ejected by its progenitor ( $\rho(r) \propto r^{-2}$ ). For instance, Eq. 14 for  $k = 0$  can be obtained from  $E \propto n \Gamma_0^\epsilon \Gamma^{8-\epsilon} t^3$  and  $\Gamma = \Gamma_0 \left( \frac{t}{t_{\text{dec}}} \right)^{-\frac{3}{8-\epsilon}}$  with  $t_{\text{dec}}$  the deceleration time scale. In this scenario, the evolution of the radiative parameters ( $\epsilon, s$ ) is related through

$$\begin{aligned} (3 + s)(8 - \epsilon) - 24 &= 0, & \text{for } k = 0 \\ (1 + s)(4 - \epsilon) - 4 &= 0, & \text{for } k = 2, \end{aligned} \quad (15)$$

where the parameter  $s$  lies in the range of  $0 \leq s \leq 3/7$  and  $0 \leq s \leq 1/3$  for the homogeneous and stellar wind medium, respectively.

### 2.4 Klein-Nishina effects

A direct effect on the SSC spectrum due to the KN regime is the suppression of up-scattered synchrotron photons, and an indirect effect occurs when the SSC emission dominates, and at least some of the injected electrons with different Lorentz factors have enough time to cool down. The SSC spectra could have several breaks depending on the location of the spectral breaks in the KN regime;  $h\nu_{\text{KN}}^{\text{syn}}(\gamma_m) \simeq \frac{2\Gamma}{(1+z)} \frac{m_e c^2}{\gamma_m}$  for  $\nu_c^{\text{syn}} < \nu_m^{\text{syn}}$  and  $h\nu_{\text{KN}}^{\text{syn}}(\gamma_c) \simeq \frac{2\Gamma}{(1+z)} \frac{m_e c^2}{\gamma_c}$  for  $\nu_m^{\text{syn}} < \nu_c^{\text{syn}}$  (see Nakar et al. 2009; Wang et al. 2010). For example, the value of the Compton parameter in the case of the slow-cooling regime ( $\nu_m^{\text{syn}} < \nu_c^{\text{syn}}$ ) might not be constant and be defined by

$$Y(\gamma_c)[Y(\gamma_c) + 1] = \frac{\epsilon_e}{\epsilon_B} \left( \frac{\gamma_c}{\gamma_m} \right)^{2-p} \begin{cases} \left( \frac{\nu_m^{\text{syn}}}{\nu_c^{\text{syn}}} \right)^{-\frac{p-3}{2}} \left( \frac{\nu_{\text{KN}}^{\text{syn}}(\gamma_c)}{\nu_m^{\text{syn}}} \right)^{\frac{4}{3}} & \text{for } \nu_{\text{KN}}^{\text{syn}}(\gamma_c) < \nu_m^{\text{syn}} \\ \left( \frac{\nu_{\text{KN}}^{\text{syn}}(\gamma_c)}{\nu_c^{\text{syn}}} \right)^{-\frac{p-3}{2}} & \text{for } \nu_m^{\text{syn}} < \nu_{\text{KN}}^{\text{syn}}(\gamma_c) < \nu_c^{\text{syn}} \\ 1 & \text{for } \nu_c^{\text{syn}} < \nu_{\text{KN}}^{\text{syn}}(\gamma_c). \end{cases} \quad (16)$$

The last cooling condition ( $\nu_c^{\text{syn}} < \nu_{\text{KN}}^{\text{syn}}(\gamma_c)$ ) corresponds to the Thomson regime, and then KN effects are neglected. In this case, the value of the Compton parameter becomes

$$Y(\gamma_c)[Y(\gamma_c) + 1] = \eta \begin{cases} \frac{\epsilon_e^{p-1}}{\epsilon_B} \left[ \frac{m_p \bar{g} \Gamma}{m_e \gamma_M} \right]^{\bar{g}} & \text{for } 1 < p < 2 \\ \frac{\epsilon_e}{\epsilon_B} & \text{for } 2 \leq p, \end{cases} \quad (17)$$

with  $\eta = 1$  and  $\left( \frac{\gamma_c}{\gamma_m} \right)^{2-p}$  for the fast- and slow-cooling regime, respectively (Sari & Esin 2001). Due to the terms  $h\nu_{\text{KN}}^{\text{syn}}(\gamma_m)$  and  $h\nu_{\text{KN}}^{\text{syn}}(\gamma_c)$  and the electron Lorentz factors (Eqs. 1 and 5), the SSC spectral breaks in the KN regime can be written explicitly as

$$\begin{aligned}
h\nu_{m,KN}^{\text{SSC}} &= \begin{cases} 4.6 \times 10 \text{ GeV } \tilde{g}^{\frac{1}{p-1}} \left( \frac{1+z}{1.1} \right)^{\frac{6-p-2\epsilon+p\epsilon}{2(p-1)(4-\epsilon)}} \mathcal{E}_{e,-1}^{\frac{1}{p-1}} \mathcal{E}_{B,-4}^{\frac{2-p}{4(p-1)}} A_{W,-1}^{\frac{12-10p+\epsilon(p-2)}{4(p-1)(4-\epsilon)}} E_{53}^{\frac{3p-2}{2(p-1)(4-\epsilon)}} \Gamma_{0,2}^{-\frac{\epsilon(3p-2)}{2(4-\epsilon)(p-1)}} t_{4.7}^{\frac{p-6-\epsilon(p-2)}{2(4-\epsilon)(p-1)}} & \text{for } 1 < p < 2 \\ 1.5 \times 10^2 \text{ GeV } g \left( \frac{1+z}{1.1} \right)^{\frac{2}{4-\epsilon}} \mathcal{E}_{e,-1} A_{W,-1}^{-\frac{2}{4-\epsilon}} E_{53}^{\frac{2}{4-\epsilon}} \Gamma_{0,2}^{-\frac{2\epsilon}{4-\epsilon}} t_{4.7}^{-\frac{2}{4-\epsilon}} & \text{for } 2 \leq p \end{cases} \\
h\nu_{c,KN}^{\text{SSC}} &= 7.1 \times 10^2 \text{ GeV} \left( \frac{1+z}{1.1} \right)^{\frac{\epsilon-2}{4-\epsilon}} (1+Y(\gamma_c))^{-1} \mathcal{E}_{B,-4}^{-1} A_{W,-1}^{\frac{\epsilon-6}{4-\epsilon}} E_{53}^{\frac{2}{4-\epsilon}} \Gamma_{0,2}^{-\frac{2\epsilon}{4-\epsilon}} t_{4.7}^{\frac{2-\epsilon}{4-\epsilon}}, \quad (18)
\end{aligned}$$

for a stellar-wind environment, and as

$$\begin{aligned}
h\nu_{m,KN}^{\text{SSC}} &= \begin{cases} 1.6 \text{ GeV } \tilde{g}^{\frac{1}{p-1}} \left( \frac{1+z}{1.1} \right)^{\frac{3(p+2)}{2(p-1)(8-\epsilon)}} \mathcal{E}_{e,-1}^{\frac{1}{p-1}} \mathcal{E}_{B,-4}^{-\frac{p-2}{4(p-1)}} n^{\frac{12-10p+\epsilon(p-2)}{4(p-1)(8-\epsilon)}} E_{53}^{\frac{p+2}{2(p-1)(8-\epsilon)}} \Gamma_{0,2}^{-\frac{\epsilon(p+2)}{2(8-\epsilon)(p-1)}} t_{4.7}^{-\frac{3(p+2)}{2(8-\epsilon)(p-1)}} & \text{for } 1 < p < 2 \\ 5.9 \text{ GeV } g \left( \frac{1+z}{1.1} \right)^{\frac{6}{8-\epsilon}} \mathcal{E}_{e,-1} n^{-\frac{2}{8-\epsilon}} E_{53}^{\frac{2}{8-\epsilon}} \Gamma_{0,2}^{-\frac{2\epsilon}{8-\epsilon}} t_{4.7}^{-\frac{6}{8-\epsilon}} & \text{for } 2 \leq p \end{cases} \\
h\nu_{c,KN}^{\text{SSC}} &= 2.7 \times 10 \text{ GeV} \left( \frac{1+z}{1.1} \right)^{\frac{2-\epsilon}{8-\epsilon}} (1+Y(\gamma_c))^{-1} \mathcal{E}_{B,-4}^{-1} n^{\frac{\epsilon-6}{8-\epsilon}} E_{53}^{-\frac{2}{8-\epsilon}} \Gamma_{0,2}^{\frac{2\epsilon}{8-\epsilon}} t_{4.7}^{\frac{\epsilon-2}{8-\epsilon}}, \quad (19)
\end{aligned}$$

for a constant-density medium. It should be noted that the total cross section in the KN regime can be approximated by  $\sigma \approx 3/8\sigma_T x^{-1} (\ln 2x + 1/2)$  with  $x = hv/m_e \gg 1$  (Rybicki & Lightman 1986).

## 2.5 Analysis and Discussion

Based on the external FS scenario, we have presented a general analytical model of the synchrotron and SSC processes in three cases: i) the fully adiabatic ( $\epsilon = 0$ ), ii) fully radiative ( $\epsilon = 1$ ), and iii) partially radiative or adiabatic ( $0 < \epsilon < 1$ ) regimes. We plotted the expected light curves and spectra for an electron spectral index  $1 < p < 2$  and  $2 \leq p$  when the outflow decelerates in a stellar wind (see Figure A1). Significant variations of the spectral and temporal features of the afterglow emission are introduced by radiative losses only if  $\epsilon$  is large and approaches to unity. In particular, when  $\epsilon = 0$ , the synchrotron and SSC light curves derived in the standard FS scenario are recovered (Bhattacharya 2001; Sari et al. 1998; Sari & Esin 2001; Fraija et al. 2019b). We want to highlight the synchrotron and SSC spectral breaks and light curves for  $1 < p < 2$  and  $2 \leq p$  become equal when  $p \rightarrow 2$ .

We have obtained and shown in Table A1 the closure relations that describe the evolution of the synchrotron and SSC flux ( $F_\nu \propto t^{-\alpha} \nu^{-\beta}$ ) as a function of  $\epsilon$  and  $p$ . The cooling conditions in the constant density medium of  $\nu_m^{\text{SSC}} \leq \nu \leq \nu_c^{\text{SSC}}$ , and  $\{\nu_m^{\text{SSC}}, \nu_c^{\text{SSC}}\} < \nu$  for  $1 < p < 2$ , are the only ones where the SSC fluxes do not depend on  $p$ , hence their closure relations cannot be estimated. In this case, the SSC flux evolves as  $\propto t^{-\alpha}$  with  $\alpha = \frac{7+4\epsilon}{8-\epsilon}$  and  $\frac{2(4+\epsilon)}{8-\epsilon}$  for the spectral indices  $\beta = \frac{p-1}{2}$  and  $\frac{p}{2}$ , respectively. Note that adiabatic breaks are expected around the transition time between the fast- and slow-cooling regimes. The transition time refers to the temporal interval of applicability of the synchrotron and SSC light curves. Given the closure relations (see Table A1), we can notice that the synchrotron and SSC fluxes will evolve similarly in time and energy if the condition  $\alpha_{\text{syn}}(\beta) \approx \alpha_{\text{SSC}}(\beta)$  is satisfied. Considering both, the stellar wind and the homogeneous afterglow model, this condition is satisfied when the observed frequency evolves in  $\{\nu_m^j, \nu_c^j\} < \nu$  (with  $j = \text{syn}$  and  $\text{SSC}$ ) and  $\beta \rightarrow 1$  (i.e.,  $p \rightarrow 2$ ). Irrespective of whether  $p$  approaches the value of 2 from  $1 < p < 2$  (e.g.  $p \approx 1.98$ ) or from  $2 \leq p$  (e.g.  $p \approx 2.02$ ), the temporal decay indices become  $\alpha \approx \frac{4}{4-\epsilon}$  and  $\approx \frac{2(4+\epsilon)}{8-\epsilon}$  for the wind and constant-density afterglow model, respectively. In the particular case of  $\epsilon \approx 0$ , the expected flux obtained from the stellar-wind and constant-density afterglow model evolves with the same temporal index of  $\alpha \approx 1$ . The temporal and spectral similarities that could be observed during the afterglow phase in two or more different bands could be interpreted in the synchrotron and SSC FC scenario with a hard spectral index  $p \approx 2$ , and the parameter  $\epsilon$  would be useful to discriminate between the stellar wind or homogeneous afterglow model. One of the more relevant features to be observed in the radiative regime should occur during the afterglow transition between a stellar wind and a constant-density medium. For  $\epsilon = 0$ , the X-ray flux evolving in the stellar wind and constant density afterglow has the same temporal evolution  $t^{-\frac{3p-2}{4}}$  when  $p$  lies in the range of  $2 < p$ . Therefore, depending on the values of observable quantities and parameters, a transition between stellar-wind and homogeneous medium afterglow could be noticeable. For an electron spectral index that does not deviate from 2 (i.e.,  $p \sim 2$ ), the expected synchrotron and SSC fluxes would evolve as  $F_\nu \propto t^{-\alpha}$  with  $\alpha = 1$  for any value of  $p$ . In this case, a transition between stellar-wind and constant-density afterglow could not be noticeable in the SSC and synchrotron light curves. Otherwise, this transition could be more highlighted as  $p$  deviates from 2 and  $\epsilon$  from 0. On the other hand, the development of the FS in the fully radiative ( $\epsilon = 1$ ) or partially radiative or adiabatic ( $0 < \epsilon < 1$ ) regimes presents an X-ray flux that has different evolution. Regardless of the values, a transition between stellar wind and homogeneous medium afterglow must be observed.

Deviations around  $\epsilon = 0$  will also modify the evolution of synchrotron and SSC spectral breaks, producing distinct variations in the afterglow tails. The SSC and synchrotron spectral breaks for  $1 < p < 2$  ( $2 < p$ ) evolve as  $\nu_m^{\text{SSC}} \propto t^{\frac{3(\epsilon-4)-p(\epsilon-2)}{(4-\epsilon)(p-1)}} (t^{\frac{\epsilon-8}{4-\epsilon}})$ ,  $\nu_m^{\text{syn}} \propto t^{\frac{\epsilon-p-4}{(4-\epsilon)(p-1)}} (t^{\frac{\epsilon-6}{4-\epsilon}})$ ,  $\nu_c^{\text{SSC}} \propto t^{\frac{8-3\epsilon}{4-\epsilon}}$  and  $\nu_c^{\text{syn}} \propto t^{\frac{2-\epsilon}{4-\epsilon}}$  for a stellar wind medium, and as  $\nu_m^{\text{SSC}} \propto t^{-\frac{18}{(8-\epsilon)(p-1)}} (t^{-\frac{18}{8-\epsilon}})$ ,  $\nu_m^{\text{syn}} \propto t^{-\frac{3(p+2)}{(8-\epsilon)(p-1)}} (t^{-\frac{12}{8-\epsilon}})$ ,  $\nu_c^{\text{SSC}} \propto t^{\frac{2(2\epsilon-1)}{8-\epsilon}}$  and  $\nu_c^{\text{syn}} \propto t^{\frac{2(\epsilon-2)}{8-\epsilon}}$  for a constant-density medium. For instance, considering  $2 < p$  the spectral breaks in the stellar wind (constant-density) medium evolve under the cooling condition  $\nu_m^{\text{syn}} \propto t^{-[1.50-1.67]} (t^{-[1.50-1.71]})$ ,  $\nu_c^{\text{syn}} \propto t^{[0.33-0.50]} (t^{-[0.29-0.50]})$ ,  $\nu_m^{\text{SSC}} \propto t^{-[2.0-2.33]} (t^{-[2.25-2.51]})$  and

$\nu_c^{\text{SSC}} \propto t^{[1.67-2.0]} (t^{[-0.25-0.29]})$  instead of the typical evolution of spectral breaks of  $\nu_m^{\text{syn}} \propto t^{-\frac{3}{2}} (t^{-\frac{3}{2}})$ ,  $\nu_c^{\text{syn}} \propto t^{-\frac{1}{2}} (t^{\frac{1}{2}})$ ,  $\nu_m^{\text{SSC}} \propto t^{-2} (t^{-\frac{5}{2}})$  and  $\nu_c^{\text{SSC}} \propto t^{-2} (t^{-\frac{1}{4}})$ , respectively.

Figures A1 and A2 illustrate the light curves and spectra of the SSC process evolving in stellar-wind and homogeneous medium for typical GRB afterglow parameters, respectively. These light curves and spectra are shown at 1 TeV and at  $5 \times 10^4$  s, respectively, for  $\epsilon_e = \epsilon$ ,  $\epsilon_B = 10^{-4}$  and different spectral indices ( $p = 1.7, 1.9, 2.1$  and  $2.3$ ). These panels are shown from top to bottom for  $\epsilon = 0, 0.2$  and  $0.4$ , and from left to right for the values of  $[A_W (n); E] = [0.1 (0.1 \text{ cm}^{-3}); 10^{52} \text{ erg}]$ ,  $[10^{-3} (10^{-3} \text{ cm}^{-3}); 10^{52} \text{ erg}]$ , and  $[10^{-3} (10^{-3} \text{ cm}^{-3}); 10^{53} \text{ erg}]$ . We consider a hypothetical burst located at  $z = 0.1$  and the model of the Extragalactic Background Light (EBL) absorption proposed in Franceschini & Rodighiero (2017). The left-hand panels in Figure A1 show that, depending on the parameter values, the expected flux will have a different behavior. For example, the light curves during the early time show a plateau phase followed by a normal decay for  $2 \leq p$ , but only in a few cases for  $1 < p < 2$ . It is also shown that irrespective of the value of the spectral index  $p$  and the parameter  $\epsilon$ , the expected flux increases as  $E$  also increases. The panels show that the expected flux  $F_\nu^{\text{SSC}} \propto t^{-\alpha}$  evolves from  $1.03 \leq \alpha \leq 1.13$  ( $1.10 \leq \alpha \leq 1.22$ ) to  $2.03 \leq \alpha \leq 2.08$  ( $2.10 \leq \alpha \leq 2.16$ ) for  $p = 1.9$  ( $p = 2.1$ ). This is due to the evolution of the SSC spectral breaks;  $\nu_m^{\text{SSC}} \propto t^{-\alpha}$  with  $1.64 \leq \alpha \leq 1.70$  ( $1.50 \leq \alpha \leq 1.56$ ) for  $p = 1.9$  ( $p = 2.1$ ), and  $\nu_c^{\text{SSC}} \propto t^{-\alpha}$  with observe that the expected flux increases in some panels as  $A_W$  increases and in other panels when  $A_W$  decreases. This result can be explained in terms of the density parameter and the cooling condition. Given the spectral index in the range  $1 < p < 2$  ( $2 \leq p$ ), the expected flux as a function of the density parameter is  $F_\nu \propto A_W^{\frac{52-8p-13\epsilon+p\epsilon}{4(4-\epsilon)}} (A_W^{\frac{44-9\epsilon-p(4+\epsilon)}{4(4-\epsilon)}})$  for  $\nu_m^{\text{SSC}} < \nu < \nu_c^{\text{SSC}}$  and  $\propto A_W^{\frac{16-8p-6\epsilon+p\epsilon}{4(4-\epsilon)}} (A_W^{\frac{8-2\epsilon-p(4+\epsilon)}{4(4-\epsilon)}})$  for  $\nu_m^{\text{SSC}} < \nu_c^{\text{SSC}} < \nu$ . Considering the value of  $p = 1.9$  ( $2.1$ ), the expected flux as a function of the density parameter is  $F_\nu \propto A_W^{\alpha_w}$  with  $2.3 \leq \alpha_w \leq 2.25$  ( $2.23 \leq \alpha_w \leq 2.16$ ) for  $\nu_m^{\text{SSC}} < \nu < \nu_c^{\text{SSC}}$  and  $-0.05 \leq -\alpha_w \leq 0.06$  ( $0.03 \leq -\alpha_w \leq 0.14$ ) for  $\nu_m^{\text{SSC}} < \nu_c^{\text{SSC}} < \nu$ . Therefore, as  $A_W$  increases, the expected flux increases if it evolves in the cooling condition  $\nu_m^{\text{SSC}} < \nu < \nu_c^{\text{SSC}}$  and decreases if it evolves in  $\nu_m^{\text{SSC}} < \nu_c^{\text{SSC}} < \nu$ . The left-hand panels in Figure A2 exhibit a similar behavior to those shown in Figure A1. For example, the evolution of the expected flux  $F_\nu^{\text{SSC}} \propto t^{-\alpha}$  from  $0.88 \leq \alpha \leq 1.13$  ( $0.99 \leq \alpha \leq 1.25$ ) to  $1.0 \leq \alpha \leq 1.16$  ( $1.11 \leq \alpha \leq 1.28$ ) for  $p = 1.9$  ( $2.1$ ) can be interpreted in terms of SSC spectral breaks;  $\nu_m^{\text{SSC}} \propto t^{-\alpha}$  with  $1.63 \leq \alpha \leq 1.71$  ( $1.50 \leq \alpha \leq 1.58$ ) for  $p = 1.9$  ( $2 \leq p$ ), and  $\nu_c^{\text{SSC}} \propto t^{-\alpha}$  with  $0.42 \leq \alpha \leq 0.50$ . Similarly, the variation of the expected flux as a function of the density can be explained in terms of the cooling condition. In the case of  $1 < p < 2$  ( $2 \leq p$ ), the expected flux is  $F_\nu \propto n^{\frac{52-8p-13\epsilon+p\epsilon}{4(8-\epsilon)}} (n^{\frac{44-9\epsilon-p(4+\epsilon)}{4(8-\epsilon)}})$  for  $\nu_m^{\text{SSC}} < \nu < \nu_c^{\text{SSC}}$  and  $\propto n^{\frac{6-8p-6\epsilon+p\epsilon}{4(8-\epsilon)}} (n^{\frac{8-2\epsilon-p(4+\epsilon)}{4(8-\epsilon)}})$  for  $\nu_m^{\text{SSC}} < \nu_c^{\text{SSC}} < \nu$ . Considering the value of  $p = 1.9$  ( $2.1$ ), the expected flux as a function of the density is  $F_\nu \propto n^{\alpha_w}$  with  $1.15 \leq \alpha_w \leq 1.06$  ( $1.11 \leq \alpha_w \leq 1.03$ ) for  $\nu_m^{\text{SSC}} < \nu < \nu_c^{\text{SSC}}$  and  $0.29 \leq -\alpha_w \leq 0.36$  ( $0.01 \leq -\alpha_w \leq 0.07$ ) for  $\nu_m^{\text{SSC}} < \nu_c^{\text{SSC}} < \nu$ . The right-hand panels in Figures A1 and A2 show the SSC spectra with the CTA (Southern array, green line), MAGIC (purple line) and *Fermi*/LAT (red line) sensitivities between 75 and 250 GeV at  $3 \times 10^4$  s for a zenith angle of  $20^\circ$  (Fioretti et al. 2019). These panels display that whereas all the expected fluxes are below the *Fermi*/LAT sensitivity, only some of them are above of the Cherenkov Telescope Array (CTA) or the Major Atmospheric Gamma-ray Imaging Cherenkov Telescop (MAGIC) Telescopes; depending on the set of parameter values. For example, the expected flux could be detected in both MAGIC and CTA for  $[A_W = 0.1 (n = 0.1 \text{ cm}^{-3}); E = 10^{52} \text{ erg}]$ , and not be detected by MAGIC or CTA for  $[10^{-3} (10^{-3} \text{ cm}^{-3}); 10^{52} \text{ erg}]$ . Given the values of  $[10^{-3} (10^{-3} \text{ cm}^{-3}); 10^{53} \text{ erg}]$ , we can see that the expected flux could be detected by CTA for  $p = 2.1$  and  $2.3$ , but not for  $p = 1.7$  or  $1.9$ . In the former case, MAGIC could not detect the expected flux for any parameter values.

### 3 APPLICATION: 2FLGC

#### 3.1 Our representative sample of GRBs

In order to apply the current model, we select those GRBs from the 2FLGC (Ajello et al. 2019b) with values of temporal and spectral indices with  $\alpha_L \geq 1.5$  and  $\Gamma_L \approx 2$  (see Table A2), which can hardly be described with closure relations of the standard synchrotron afterglow model, and also exhibit energetic photons above the synchrotron limit (e.g., see Ghisellini et al. 2010; Tak et al. 2019; Fraija et al. 2022a). Our sample is formed by ten bursts (one short GRB and nine long GRBs), seven of which have a measured redshift. We briefly describe the multi-wavelength observations of our representative sample of GRBs.

##### 3.1.1 GRB 080825C

On 25 August 2008 at 14:13:48 UT, the Gamma-ray Burst Monitor (GBM) instrument on board the *Fermi* telescope was triggered by GRB 080825C (van der Horst & Connaughton 2008a). The initial estimation set a duration of  $T_{90} = 23$  s (van der Horst & Connaughton 2008b). Nevertheless, further spectral analysis of the data from *Fermi*/GBM, revealed that the main emission lasted  $T_{90} = 27$  s in the energy band 8 – 1000 keV (Abdo et al. 2009b). The fluence measured by the GBM instrument was  $(0.11 \pm 0.04) \times 10^{-5} \text{ erg cm}^{-2}$ . Moreover, this burst is the first detection of the *Fermi*/LAT instrument of a GRB (Bouvier et al. 2008; Moretti & Axelsson 2016). During all the emission, the photons had energies below 1 GeV (Bouvier et al. 2008). No redshift was associated to this event.

The circumburst medium remains unconstrained for this burst due to the absence of X-ray and optical data.



### 3.1.2 GRB 090510

GRB 090510 was detected by the Burst Alert Telescope (BAT) instrument on board the *Neil Gehrels Swift Observatory* and by the *Fermi*/LAT instrument. Subsequently, the other instruments of both facilities observed the field of GRB 090510 (De Pasquale et al. 2010; Ukwatta et al. 2009). The duration of this burst was estimated to be  $T_{90} = 0.3 \pm 0.1$  s (Ukwatta et al. 2009; De Pasquale et al. 2010), with a corresponding fluence  $(1.7 \pm 0.6) \times 10^{-5}$  erg cm $^{-2}$  and isotropic energy of  $E_{\gamma, \text{iso}} = (5.8 \pm 0.5) \times 10^{53}$  erg (Ajello et al. 2019a). Due to the large energy released by this event, *Fermi*/LAT reported 12 photons with energy greater than 1 GeV during the first three seconds after the trigger. Spectroscopic data from the Very Large Array (VLA) allowed to estimate a redshift of  $z = 0.903$  from the OII and H $\beta$  lines (Rau et al. 2009).

De Pasquale et al. (2010); Nicuesa Guelbenzu et al. (2012) analyzed the X-ray and UV/optical/IR afterglow observations of GRB 090510. Given the SMC dust extinction with  $A_V^{\text{host}} = 0.17^{+0.21}_{-0.17}$  mag, they reported early temporal and spectral indices of  $\alpha_X = 0.74 \pm 0.03$  and  $\alpha_{\text{Opt},1} \approx -0.2 \pm 0.2$  evolving to  $\alpha_{\text{Opt},2} = 0.80 \pm 0.1$ , and  $\beta_X = 0.8 \pm 0.1$  and  $\beta_{\text{Opt}} = 0.85 \pm 0.05$  for X-ray and UV-optical-IR observations, respectively. The closure relations of the temporal and spectral indices of late X-ray and optical observations are  $F_{\nu, X} \propto t^{-0.74, 30 \pm 0.03} \nu^{-0.8 \pm 0.1}$  and  $F_{\nu, \text{Opt}} \propto t^{-0.80 \pm 0.1} \nu^{-0.85 \pm 0.05}$ , respectively. Although, the closure relations are similar to each other, the evolution in a constant-density medium under the condition  $\nu_m^{\text{syn}} < \nu_{\text{Opt}} < \nu_X < \nu_c^{\text{syn}}$  is more favorable for  $p \approx 2.4 \pm 0.2$  or  $p \approx 2.6 \pm 0.2$ , respectively. The evolution in stellar-wind environment in the same cooling condition leads to an atypical value of the spectral index with  $p < 1.4$ .

### 3.1.3 GRB 090902B

GRB 090902B was detected by the *Fermi*/GBM instrument on 2 September 2009 at 11:05:08.31 UTC. The duration of this burst was estimated to be  $T_{90} = 19.33$  s, with a corresponding fluence of  $(7.0 \pm 1.0) \times 10^{-5}$  erg cm $^{-2}$  and isotropic energy of  $E_{\gamma, \text{iso}} = (3.7 \pm 0.3) \times 10^{53}$  erg (Ajello et al. 2019a). This bright event was within the *Fermi*/LAT field of view initially at an angle of  $51^\circ$  from the line of sight, and therefore this instrument showed an increment correlated with the *Fermi*/GBM trigger. Later, GRB 090902B was detected by the X-ray Telescope (XRT) (Kennea & Stratta 2009), and by the Ultraviolet/Optical Telescope (UVOT) instruments (Swenson & Siegel 2009) on board the *Neil Gehrels Swift Observatory*, as well as by several other ground-based telescopes. The spectrum obtained with the Gemini-North telescope (Cucchiara et al. 2009) showed a series of metal absorption features corresponding to a redshift of  $z = 1.822$  (Cucchiara et al. 2009).

Pandey et al. (2010) conducted an analysis of the X-ray and UV-optical-IR afterglow data associated with GRB 090902B. Given the SMC-like dust extinction with  $A_V^{\text{host}} = 0.20 \pm 0.06$ , the authors performed a temporal and spectral analysis resulting in early temporal indices of  $\alpha_X = 1.30 \pm 0.04$  and  $\alpha_{\text{Opt}} \approx 1.60$ , and  $\beta_X = 0.9 \pm 0.1$  and  $\beta_{\text{Opt}} = 0.68 \pm 0.11$  for X-ray and UV-optical-IR observations, respectively. The closure relations of the temporal and spectral indices of late X-ray and optical observations are  $F_{\nu, X} \propto t^{-1.30 \pm 0.04} \nu^{-0.9 \pm 0.1}$  and  $F_{\nu, \text{Opt}} \propto t^{-1.60} \nu^{-0.68 \pm 0.11}$ , respectively. The fact that the temporal (spectral) index for the optical observations is larger (lower) than the X-ray observations indicates that the closure relations of the synchrotron FS model evolve in a slow cooling regime through a wind-like medium ( $\nu_m^{\text{syn}} < \nu_{\text{Opt}} < \nu_c^{\text{syn}} < \nu_X$ ) for  $p \approx 2.3 \pm 0.3$ .

### 3.1.4 GRB 090926A

The *Fermi*/GBM triggered on GRB 090926A at 04:20:26.99 UTC on 26 September 2009 (Ackermann et al. 2011). The duration of this burst was estimated to be around  $T_{90} = 20$  s (Bissaldi 2009), whereas the isotropic energy was measured as  $E_{\gamma, \text{iso}} = (3.7 \pm 0.3) \times 10^{53}$  erg (Golenetskii et al. 2009). Ackermann et al. (2011) analyzed data from the *Fermi*/LAT and *Fermi*/GBM instruments for GRB 090926A, concluding the presence of a characteristic high-energy power law component. The photometry data set includes observations from *Swift*/XRT, *INTEGRAL*/SPI-ACS (Bissaldi 2009), *Suzaku*/WAM (Noda et al. 2009), *CORONAS*/Photon (Chakrabarti et al. 2009), the Konus-wind experiment (Golenetskii et al. 2009) and the *Swift*/UVOT (Malesani et al. 2009) instruments. Using data from the *VLT*/X-shooter Malesani et al. (2009) estimated a redshift of  $z = 2.11$ .

Swenson et al. (2010) and Cenke et al. (2011) performed a temporal and spectral analysis of X-ray and optical data including UVOT observations from GRB 090926A. They reported temporal indices of  $\alpha_X = 1.43 \pm 0.03$  and  $\alpha_{\text{Opt}} \approx 1.01^{+0.07}_{-0.03}$ , and spectral indices of  $\beta_X = 1.12 \pm 0.13$  and  $\beta_{\text{Opt}} = 0.88 \pm 0.07$  for X-ray and UV-optical-IR observations, respectively. The closure relations of the temporal and spectral indices of early X-ray and optical observations are  $F_{\nu, X} \propto t^{-1.43 \pm 0.03} \nu^{-1.12 \pm 0.13}$  and  $F_{\nu, \text{Opt}} \propto t^{-1.01^{+0.07}_{-0.03}} \nu^{-0.88 \pm 0.07}$ , respectively. The fact that the temporal (spectral) index for the X-ray observations is greater than the optical observations suggests that the closure relations of the synchrotron FS model evolve in a slow cooling regime through a homogeneous medium ( $\nu_m^{\text{syn}} < \nu_{\text{Opt}} < \nu_c^{\text{syn}} < \nu_X$ ) for  $p \approx 2.5 \pm 0.2$ .

### 3.1.5 GRB 110731A

The *Fermi*/GBM instrument detected GRB 110731A on 31 July 2011 (Malesani et al. 2009), estimating a duration of  $T_{90} = 7.49$  s (Gruber 2011). Independently, *Swift*/BAT triggered on this event about 30 s after the initial *Fermi*/GBM trigger. Ackermann et al. (2013) calculated the isotropic energy measured using a power law and a band function model, obtaining  $E_{\gamma, \text{iso}} = (7.6 \pm 0.2) \times 10^{53}$  erg. The *Swift*/XRT and the *Swift*/UVOT instruments began to observe the field of GRB 110731A a time  $T + 66.4$  s and  $T + 75$  s after the *Swift*/BAT trigger, respectively (Oates et al. 2011). Due to the energy of this event, several ground facilities followed up this GRB, such as the Faulkes Telescopes North and South (Bersier 2011), the Nordic Optical Telescope equipped with ALFOSC (Malesani et al. 2011), Konus-Wind (Golenetskii et al. 2011),

the EVLA (Zauderer et al. 2011), the Suzaku Wide-band All-sky Monitor (WAM) (Hanabata et al. 2011) and the SAO RAS and Terskol observatories (Moskvitin et al. 2011). The redshift value was determined to be  $z = 2.83$  using spectroscopic observations with the GMOS-N instrument on Gemini-North (Tanvir et al. 2011).

Ackermann et al. (2013) conducted an analysis of the X-ray and UV/optical afterglow data associated with GRB 110731A. After performing an analysis of the broadband spectral energy distribution (SED), the authors presented the spectral indices of  $\beta_X = 0.95^{+0.07}_{-0.09}$  and  $\beta_{\text{Opt}} = 0.45^{+0.07}_{-0.09}$  for X-ray and UV/optical observations, at a time interval of 550 s. Similarly, the temporal analysis led to X-ray and optical indices of  $\alpha_X = 1.10 \pm 0.02$  and  $\alpha_{\text{Opt}} = 1.37 \pm 0.03$ , respectively. The closure relations of the temporal and spectral indices of late X-ray and optical observations are  $F_{\nu,X} \propto t^{-1.10 \pm 0.02} \nu^{-0.95^{+0.07}_{-0.09}}$  and  $F_{\nu,\text{Opt}} \propto t^{-1.37 \pm 0.03} \nu^{-0.45^{+0.07}_{-0.09}}$ , respectively. The fact that the temporal (spectral) index for the optical observations is greater (smaller) than the one for the X-ray observations indicates that the closure relations of the synchrotron FS model evolve in a slow cooling regime going through a wind-like medium ( $\nu_m^{\text{syn}} < \nu_{\text{Opt}} < \nu_c^{\text{syn}} < \nu_X$ ) for  $p \approx 2.15 \pm 0.15$ .

### 3.1.6 GRB 130502B

On 2 May 2013 at 07:51:11.76 UT, the *Fermi*/GBM instrument was triggered by GRB 130502B. The estimated duration in the 50 – 300 keV energy band was measured to be  $T_{90} = 24$  s (von Kienlin & Younes 2013). The GBM fluence was  $(0.5 \pm 0.2) \times 10^{-5}$  erg cm $^{-2}$  (Ajello et al. 2019a). In the follow-up campaign after the initial GBM trigger, some of the instruments involved which observed the field of GRB 130502B include the *Fermi*/LAT, *Swift*/XRT, *Swift*/UVOT, P60 and Konus-Wind (Cenko et al. 2013; Breeveld & Immler 2013; Melandri & Immler 2013; Kocevski et al. 2013).

The best-fit values of temporal and spectral indices derived by the Swift team and shown in the *Swift*/XRT repository  $\alpha_X = 1.62^{+0.27}_{-0.26}$  and  $\beta_X = 0.76^{+0.20}_{-0.19}$  are used.<sup>3</sup> Due to a lack of optical observations, the circumburst media for this burst, can not be restricted.

### 3.1.7 GRB 141207A

The *Fermi*/GBM and *Fermi*/LAT instruments were simultaneously triggered by GRB 141207A on 07 December 2017 (Burns 2014; Arimoto et al. 2014). The *Fermi*/GBM light curve exhibited a duration  $T_{90}$  of approximately 20 s in the 50 – 300 keV band. The GBM fluence was  $(2.0 \pm 0.8) \times 10^{-5}$  erg cm $^{-2}$  (Ajello et al. 2019a). The *Swift*/XRT instrument began to observe the field of GRB 141207A about  $T + 13$  hours, finding an uncatalogued X-ray source corresponding to the afterglow of this burst (Amaral-Rogers & Evans 2014).

For this burst, the circumburst environment remains unconstrained as a result of the absence of X-ray and optical data.

### 3.1.8 GRB 170214A

On 14 February 2017 at 15:34:26.92 UT, the *Fermi*/GBM was triggered by GRB 170214A. The GBM light curve showed multiple overlapping peaks with a duration  $T_{90} \sim 123$  s in the 50-300 keV energy band (Mailyan & Meegan 2017). The estimated isotropic energy was  $E_{\gamma,\text{iso}} = (32 \pm 5) \times 10^{52}$  erg and the GBM fluence was  $(0.9 \pm 0.1) \times 10^{-5}$  erg cm $^{-2}$  (Ajello et al. 2019a). The *Fermi*/LAT instrument was simultaneously triggered by this burst, and it observed more than 160 photons above 100 MeV and more than 13 photons above 1 GeV. The highest-energy event was a photon with an energy of 7.8 GeV (Racusin et al. 2017). Approximately 41 hours after the initial GBM trigger, Kruehler et al. (2017) observed the optical counterpart of the burst with the ESO Very Large Telescope UT 2 equipped with the X-shooter spectrograph. The authors claimed a redshift of  $z = 2.53$  due to various absorption features in the low-energy optical observations.

The best-fit values of temporal and spectral indices derived by the Swift team and shown in the *Swift*/XRT repository  $\alpha_X = 1.3^{+0.5}_{-0.4}$  and  $\beta_X = 0.9 \pm 0.5$  are used.<sup>4</sup> The value of the temporal index that best fits the observations collected with the optical instruments is  $\alpha_{\text{Opt}} = 1.38 \pm 0.09$ . The closure relations of the temporal and spectral indices of late X-ray and optical observations are  $F_{\nu,X} \propto t^{-1.3^{+0.5}_{-0.4}} \nu^{-0.9 \pm 0.5}$  and  $F_{\nu,\text{Opt}} \propto t^{-1.38 \pm 0.09}$ , respectively. Similar to what happened in the GRB 131108A, the spectral index does not include optical frequencies. Although, the closure relations are similar to each other, the evolution in homogeneous medium under the condition  $\nu_m^{\text{syn}} < \nu_c^{\text{syn}} < \nu_{\text{Opt}} < \nu_X$  for  $p \approx 2.4 \pm 0.2$  is more favorable due to the absence of temporal breaks in both X-ray and optical observations.

<sup>3</sup> [https://www.swift.ac.uk/xrt\\_live\\_cat/00020266/](https://www.swift.ac.uk/xrt_live_cat/00020266/), [https://www.swift.ac.uk/xrt\\_spectra/00020266/](https://www.swift.ac.uk/xrt_spectra/00020266/)

<sup>4</sup> [https://www.swift.ac.uk/xrt\\_live\\_cat/00020740/](https://www.swift.ac.uk/xrt_live_cat/00020740/), [https://www.swift.ac.uk/xrt\\_spectra/00020740/](https://www.swift.ac.uk/xrt_spectra/00020740/)

### 3.1.9 GRB 180720B

The *Fermi* and *Swift* satellites triggered on GRB 180720B at 14:21:39.65 UT on 20 July 2018 (Roberts & Meegan 2018; Bissaldi & Racusin 2018). The duration of the burst was confirmed by a posterior analysis to be  $T_{90} = 48.90$  s. The preliminary multi-peaked structure lasted beyond the available event data range of the *Swift*/BAT instrument (Barthelmy et al. 2018). The estimated isotropic energy was  $E_{\gamma, \text{iso}} = (0.39 \pm 0.09) \times 10^{52}$  erg and the GBM fluence was  $(0.19 \pm 0.05) \times 10^{-5}$  erg cm $^{-2}$  (Ajello et al. 2019a). Optical and near-infrared (NIR) follow-up of GRB 180720B began observations about  $T + 73$  s (Sasada et al. 2018). Vreeswijk et al. (2018) monitored the field of GRB 180720B with the *VLT*/X-shooter spectrograph, estimating a redshift of  $z = 0.654$  from the match of several absorption features revealed in the spectrum.

Fraija et al. (2019c) performed a temporal and spectral analysis of the X-ray and R-band optical observations of GRB 180720B. Based on early observations, the authors reported spectral indices of  $\beta_X = 0.697^{+0.010}_{-0.010}$  and  $\beta_{\text{Opt}} = 0.68 \pm 0.06$ , and temporal indices of  $\alpha_X = 1.26 \pm 0.06$  and  $\alpha_{\text{Opt}} = 1.22 \pm 0.02$  for X-ray and optical observations, respectively. The closure relations of the temporal and spectral indices of X-ray and optical observations are  $F_{\nu, X} \propto t^{-1.26 \pm 0.06} \nu^{-0.697^{+0.010}_{-0.010}}$  and  $F_{\nu, \text{Opt}} \propto t^{-1.22 \pm 0.02} \nu^{-0.68 \pm 0.06}$ , respectively. Although, the closure relations are similar to one another, the evolution in stellar-wind or constant-density medium under the condition  $\nu_m^{\text{syn}} < \nu_{\text{Opt}} < \nu_X < \nu_c^{\text{syn}}$  is more favorable for  $p \approx 2.0 \pm 0.2$  or  $p \approx 2.6 \pm 0.2$ , respectively. The evolution in the condition  $\max\{\nu_m^{\text{syn}}, \nu_c^{\text{syn}}\} < \nu_{\text{Opt}} < \nu_X$  leads to an atypical value of the spectral index with  $p < 1.5$ . The temporal break exhibited at  $2.6 \times 10^5$  s with a temporal index  $1.70 \pm 0.19$  in the X-ray light curve (Fraija et al. 2019c) is consistent with the post-jet break phase in stellar wind for  $p \approx 2.0 \pm 0.2$ .

## 3.2 Data Reduction

### 3.2.1 Fermi/LAT Data

The *Fermi*/LAT data files were retrieved from the science data repository.<sup>5</sup> The *Fermi*/LAT data set was analyzed in the 0.1–100 GeV energy range using time-resolved likelihood analysis and the *Fermi* Science tools `ScienceTools 2.2.0`.<sup>6</sup> Following the unbinned likelihood analysis presented by the *Fermi*/LAT team,<sup>7</sup> we use the responses provided by Ajello et al. (2019b) for each burst. We use the `gtselect` tool to select a region of interest (ROI) within a radius of  $15^\circ$  around the point of the burst and impose a cut on the zenith angle greater than  $100^\circ$ . Furthermore, before evaluating the ROI cut, we acquire the most relevant time intervals in the data using the `gtmktime` tool. We use diffuse components and point sources from 4FGL-DR3 (e.g., see `make4FGLxml` Abdollahi et al. 2022) to define the model required to characterize the source. Using `GALPROP g11_iem_v07` and a PL spectrum, we establish a point source at the location of this burst and a diffuse galactic component. In addition, the extragalactic background `iso_P8R3_SOURCE_V3_v1` was used.<sup>8</sup> The spectral index for each burst is set at the value stated by Ajello et al. (2019b) in Table 4. We use the tool `gtltcube` with a step  $\delta\theta = 0.025$ , a bin size of 0.5 and a maximum zenith angle of  $100^\circ$  to create a lifetime cube. We consider a region of  $30^\circ$  around the GRB position and define 100 spatial bins in longitude/latitude and 50 energy bins to create the exposure map with `gtexpmap`. Furthermore, we carry out the likelihood analysis using `pyLikelihood`.<sup>9</sup> Finally, using the `gtsrcprob` tool, we retrieve photons with a probability greater than 90% to be correlated with each burst. As follows, we describe the relevant features of the energetic photons associated with each burst.

**3.2.1.1 GRB 080825C** At 3.06 s after the trigger time, the first high-energy photon was detected with measured energy of 153.4 MeV. In this burst, there were 14 photons with energy over 100 MeV. The highest energy photon detected in the LAT data was 682.9 MeV, 28.3 s after the trigger time.

**3.2.1.2 GRB 090510** At 0.18 s after the GBM trigger, the first high-energy photon was detected with measured energy of 526.4 MeV. The energy range of the photons in this burst was extensive, with 261 photons over 100 MeV and 33 exceeding 1 GeV. At 0.82 s after the GBM trigger, the highest-energy photon in the LAT data had a measured energy of 19.9 GeV.

**3.2.1.3 GRB 090902B** The first detection of a high-energy photon occurred around 1.86 s after the trigger of the GBM, with a measured energy of 284.4 MeV. The photon energy spectrum in this burst had a wide range, with 469 photons with energies over 100 MeV, 67 photons surpassing 1 GeV, and seven photons surpassing 10 GeV. The highest-energy photon in the LAT data was measured to have an energy of 39.88 GeV at about 81.7 s after the GBM trigger.

**3.2.1.4 GRB 090926A** A photon with an energy of 130.6 MeV, the first photon in a series of high-energy photons, was seen 2.21 s after the GBM trigger. The burst under analysis exhibited a diverse spectrum of photon energies, whereby 339 photons had energies above 100 MeV, 31

<sup>5</sup> <https://fermi.gsfc.nasa.gov/cgi-bin/ssc/LAT/LATDataQuery.cgi>

<sup>6</sup> <https://fermi.gsfc.nasa.gov/ssc/data/analysis/software/>

<sup>7</sup> [https://fermi.gsfc.nasa.gov/ssc/data/analysis/scitools/likelihood\\_tutorial.html](https://fermi.gsfc.nasa.gov/ssc/data/analysis/scitools/likelihood_tutorial.html)

<sup>8</sup> <https://fermi.gsfc.nasa.gov/ssc/data/access/lat/BackgroundModels.html>

<sup>9</sup> [https://fermi.gsfc.nasa.gov/ssc/data/analysis/scitools/python\\_tutorial.html](https://fermi.gsfc.nasa.gov/ssc/data/analysis/scitools/python_tutorial.html)

possessed energies surpassing 1 GeV, and two possessed energies exceeding 10 GeV. Approximately 24.84 s after the GBM trigger, the LAT instrument detected a photon with a maximum energy of 19.46 GeV.

**3.2.1.5 GRB 110731A** The first detection of a high-energy photon, with an energy measurement of 817.1 MeV, occurred at a time interval of 3.19 s after the trigger time. A diverse range of photon energies was generated during this burst, with 40 photons over 100 MeV and an additional four photons surpassing 1 GeV. The most energetic photon seen by the LAT instrument was observed to occur 1.93 s after the trigger time, with measured energy of 8.27 GeV.

**3.2.1.6 GRB 130502B** There was a wide variety of energies present in this burst, with 68 photons having energy more than 100 MeV and 2 having energy more than 10 GeV. At 222.1 s after the GBM trigger, the highest energetic photon detected in the LAT data had an energy of 31.1 GeV, followed by a photon with an energy of 17.3 MeV detected at 48.2 s after the GBM trigger.

**3.2.1.7 GRB 141207A** The first energetic photon, measured at 765.3.5 MeV, was detected 3.9 s after the GBM trigger. In this burst, there were 19 photons with energy over 100 MeV and 11 with energies above 1 GeV. At 734.3 s after the GBM trigger, the highest energetic photon detected in the LAT data had an energy of 5.5 GeV.

**3.2.1.8 GRB 170214A** The first high-energy photon, with a measured energy of 152.5 MeV, was detected 39.5 s after the GBM trigger. A wide variety of energies was present in this burst, with 217 photons having energy more than 100 MeV and 13 having energies greater than 1 GeV. At 103.6 s after the GBM trigger, the highest energetic photon detected in the LAT data had an energy of 7.8 GeV.

**3.2.1.9 GRB 180720B** The first detection of a high-energy photon occurred 12.5 s after the BAT trigger, and its energy was measured to be 175.2 MeV. The energy spectrum of the photons in this burst exhibited a wide range, with 129 photons with energies over 100 MeV and eight photons above the threshold of 1 GeV. The LAT instrument detected the photon with a maximum energy of 142.4 s after the BAT trigger, and its energy was measured to be 4.9 GeV.

### 3.2.2 *Swift/XRT Data*

The Swift/XRT followed-up GRB 090510, 090902B, 090926A, 110731A, 130502B, 131108A, 170214A and 180720B in different series of observations (De Pasquale et al. 2010; Kennea & Stratta 2009; Ackermann et al. 2011; Oates et al. 2011; Cenko et al. 2013; Stroh & Kennea 2013; Beardmore et al. 2017; Evans 2018). This instrument monitored these bursts in the photon counting (PC) and windowed-timing (WT) modes with spectrum exposures from hundreds to hundreds of thousands of seconds. The best-fitting absorption columns (intrinsic) ranges from  $2.1_{-1.3}^{+1.4} \times 10^{21}$  to  $4.4_{-3.0}^{+3.1} \times 10^{21}$  cm<sup>-2</sup>, and from  $10_{-10.0}^{+11.2} \times 10^{20}$  to  $2.3_{-0.6}^{+0.8} \times 10^{22}$  cm<sup>-2</sup> for WT and PC modes, respectively. Data sets from the Swift/XRT instrument were obtained from the publicly accessible database of the Swift website.<sup>10</sup> The flux density at 10 keV is converted to 1 keV using the conversion factor determined in Evans et al. (2010).

### 3.2.3 *Optical Data*

Optical data for GRB 090510 (White-band), GRB 090902B (R-band), GRB 090926A (V-band), GRB 110731A (White- and V-band), GRB 131108A (White-, B-, U- and W1-band), GRB 170214A (White- and R-band) and GRB 180720B (R-band) were taken from Fraija et al. (2016b), Pandey et al. (2010), Rau et al. (2010), Fraija (2015), Ajello et al. (2019c); Giuliani et al. (2014); Corsi et al. (2013); Volnova et al. (2013b,a), Tang et al. (2017); Beardmore et al. (2017); Mazaeva et al. (2017); Kruehler et al. (2017) and Fraija et al. (2019c), respectively.

## 3.3 Results and Discussion

We use the analysis of the closure relations shown in the subsection 3.1 to describe our GRB sample with the current model evolving in the stellar wind or homogeneous environment. The panels in Figure A3 display the LAT observations of GRB 080825C, GRB 130502B, and GRB 141207A with the best-fit curve generated by the FS model evolving in the stellar wind (right) and constant density (left) environment. Due to these three bursts having unknown redshifts, we assume a value of  $z = 1.0$  to estimate the total radiated energy and the luminosity distance. We show the afterglow evolution in both the stellar wind and homogeneous environment because the circumburst environments cannot be constrained as a result of the absence of optical data for GRB 130502B and X-ray and optical data for GRB 080825C and GRB 141207A. The panels in Figure A4 show the LAT, X-ray, and optical observations of GRB 090510, GRB 090926A and GRB 170214 with the best-fit curve generated by the FS model evolving in the constant-density medium, and the panels in Figure A5 show the LAT, X-ray and optical observations of GRB 090902B, GRB 110731A and GRB 180720B with the best-fit curve generated by the FS model evolving in the stellar-wind environment. We use Markov-Chain Monte Carlo (MCMC) simulations with the eight parameters used for the complete sample of GRBs to

<sup>10</sup> [https://www.swift.ac.uk/burst\\_analyser/00922968/](https://www.swift.ac.uk/burst_analyser/00922968/)

find the best-fit values that describe the multi-wavelength afterglow observations with the SSC and synchrotron FS models. To represent all the data in this case, a total of 15900 samples and 4400 tuning steps are used. The effect of EBL absorption as proposed in [Franceschini & Rodighiero \(2017\)](#) was adopted. We only display Figure A6, which corresponds to GRB 080825C, for showing the best-fit values and the median of the parameter posterior distributions. Tables A3 and A4 list the best-fit values found with MCMC simulations after describing the multiwavelength afterglow observations with a synchrotron and SSC model evolving in both types of considered media. Tables A5 and A6 display the synchrotron and SSC spectral breaks in a constant-density and a stellar-wind medium, respectively, which are calculated with the best-fit values reported in Tables A3 and A4. We note that, while it may appear that the early LAT lightcurves are better fitted by the pure SSC model, we must also simultaneously explain the X-ray and optical observations. These are well fitted with the synchrotron model, so the synchrotron component is required and we are not able to consider a pure SSC model just for the LAT curves. Furthermore, with the parameters found, the SSC flux decreases very slowly and gives a small contribution of the early LAT data, which is less compared to the synchrotron radiation.

### 3.3.1 Microphysical parameters

The best-fit values of the microphysical parameter given to accelerate electrons lie in the range of  $0.3 \leq \epsilon_e \leq 0.9$ . In the constant-density scenario, the synchrotron afterglow model used for modeling the LAT light curves of GRB 090926A, GRB 141207A and GRB 170214A shows that they lie in the fast-cooling regime, while the light curves of GRB 080825C, GRB 090510 and GRB 130520B lie in the slow-cooling regime; see Table A5. In the stellar-wind scenario, the synchrotron afterglow model used for modeling our sample shows that the light curves lie in the fast-cooling regime; see Table A6. The results indicate that although the fraction of the total energy density given to accelerate electrons is much greater than  $\epsilon_e \gg 0.1$ , the shock-accelerated electrons are not in the fast-cooling regime during the entire LAT light curve. This indicates that for some GRBs a transition from radiative to adiabatic regime occurs at the beginning of the LAT observations.

The best-fit values of the magnetic microphysical parameter lie in the interval  $10^{-5} \leq \epsilon_B \leq 10^{-1}$ . As such, they are in the range of values required to model the multiwavelength afterglow observations in a large sample of GRBs;  $10^{-5} \lesssim \epsilon_B \lesssim 10^{-1}$  ([Wijers & Galama 1999](#); [Panaitescu & Kumar 2002](#); [Yost et al. 2003](#); [Panaitescu 2005](#); [Santana et al. 2014](#)). [Tak et al. \(2019\)](#) conducted a comprehensive analysis of temporal and spectral indices, meticulously examining the closure relations within a sample of 59 LAT-detected bursts that were carefully chosen. They showed that although the traditional synchrotron emission model adequately explains the spectrum and temporal indices in the majority of instances, a significant proportion of bursts can hardly be characterized by this model. Furthermore, they reported that those satisfying the closure relations are in the slow-cooling regime ( $\nu_m^{\text{syn}} < \nu_{\text{LAT}} < \nu_c^{\text{syn}}$ ) as long as the microphysical parameter is unusually low ( $\epsilon_B < 10^{-7}$ ). Our results show that the closure relations of a fraction of bursts can be satisfied with the synchrotron afterglow model in the radiative regime and typical values of  $\epsilon_B$ .

### 3.3.2 The post-jet-break decay phase

In a time scale of days, during the post-jet break decay phase, it is expected that the afterglow lies in the adiabatic regime rather than the radiative regime ([Racusin et al. 2009](#)). Therefore, the multi-wavelength observations could be described with  $F_\nu^{\text{syn}} \propto t^{-p}$ , for  $\nu_m^{\text{syn}} < \nu < \nu_c^{\text{syn}}$  or  $\max\{\nu_{m,f}^{\text{syn}}, \nu_{c,f}^{\text{syn}}\} < \nu$  (see e.g. [Fraija et al. 2022b](#)), which are distinct from the temporal decay indices found for our sample ([Pereyra et al. 2022](#); [Becerra et al. 2019](#)), except GRB 090510 and GRB 110731A. This implies that, except for these bursts, they were most likely emitted from a wide outflow with a significant half-opening angle, as shown by multi-wavelength observations, which display no indication of late steep decays. Based on the best-fit values, the jet opening angles become  $\gtrsim 8^\circ$ , and for GRB 090510 and GRB 110731A, they are  $\theta_j \approx 0.5^\circ$  and  $2^\circ$ , respectively, which lies in the usual values ( $\theta_j \lesssim 10^\circ$ ; [Bloom et al. 2001](#)).

### 3.3.3 Efficiency of equivalent kinetic energy

The efficiency provides crucial information on the gamma-ray emitting process. The best-fit values of the equivalent kinetic energies  $5.72 \times 10^{52} \leq E \leq 10^{54}$  erg and the isotropic energies in gamma-rays reported by the GBM and LAT instruments in the range of  $4.0 \times 10^{51} \leq E_{\gamma,\text{iso}} \leq 1.3 \times 10^{54}$  erg ([Ajello et al. 2019a](#)) lead to kinetic efficiencies in the range of  $0.03 \lesssim \eta_K \lesssim 0.32$ , which are typical compared to those values reported in the literature ([Guetta et al. 2001](#); [Zhang et al. 2007](#); [Kumar & Zhang 2015](#)), and a kinetic efficiency of  $\eta \approx 0.03$  for GRB 180720B, which is very low. The atypical value of efficiency for GRB 180720B was estimated considering the isotropic energy reported in the 2FLGC. If we would have considered the isotropic energy reported in other analyses ( $3 \times 10^{53}$  erg [Abdalla et al. 2019](#); [Fraija et al. 2019d](#)), the kinetic efficiency would have been  $\eta \approx 0.24$ .

### 3.3.4 The profile of the circumburst environment

The best-fit values of the wind parameter lie in the range of  $10^{-2} \lesssim A_W \lesssim 1$ , typical for GRBs identified as powerful bursts (Ackermann et al. 2013; Perley et al. 2014; Vestrand et al. 2014; Fraija et al. 2012; Racusin et al. 2008; Fraija et al. 2017; Becerra et al. 2017). Similarly, the values found of the homogeneous medium in the range  $4.6 \times 10^{-3} \lesssim n \lesssim 1 \text{ cm}^{-3}$  are usual with those found for other GRBs (Fraija et al. 2019c; Acciari et al. 2021; H. E. S. S. Collaboration 2021; LHAASO Collaboration 2023). Considering the fact that short bursts detonate at very low densities (Soderberg et al. 2006; Berger 2014), the value of  $n = 4.6 \times 10^{-3} \text{ cm}^{-3}$  obtained for GRB 090510 is compatible with the observations. Furthermore, the joint detection and modeling of the gravitational and electromagnetic signatures (Abbott et al. 2017b; Goldstein et al. 2017), which were associated with a fusion of two neutron stars (Abbott et al. 2017a), provided values of circumburst densities consistent with the ones obtained for GRB 130502B.

Similarly to other bursts identified by the LAT instrument and predicted values from numerical simulations (Tchekhovskoy et al. 2008), the best-fit values of the initial bulk Lorentz factor fall in the range  $10^2 \lesssim \Gamma \lesssim 10^3$ . Since our GRB sample included the highest energetic photons, we expect the bulk Lorentz factor values to coincide with those of the strongest bursts seen by the *Fermi*/LAT (Ackermann et al. 2011; Veres & Mészáros 2012; Ackermann et al. 2013; Abdo et al. 2009a; Ackermann & et al. 2010; Ackermann et al. 2014; Fraija et al. 2019a,c).

### 3.3.5 The highest energy photons

Figure A7 exhibits all photons with energies  $> 100 \text{ MeV}$  and probabilities  $> 90\%$  of being associated with each burst of our representative sample. Additionally, we show in red lines the maximum photon energies released by the synchrotron afterglow model evolving in a constant-density (dotted) and stellar-wind (dashed) environment, estimated with the best-fit values reported in Tables A3 and A4. This Figure shows that the synchrotron FS model cannot explain the highest energy photons collected by *Fermi*/LAT. Energetic photons above  $> 10 \text{ GeV}$  are usually explained via hadronic and SSC scenarios. In the hadronic scenarios, high-energy gamma-ray emission has been interpreted via photo-hadronic interactions; ultrarelativistic protons accelerated in the jet with internal synchrotron photons (Asano et al. 2009; Dermer et al. 2000), inelastic proton-neutron collisions (Mészáros & Rees 2000), and relativistic neutrons with seed photons coming from the outflow (Dermer & Atoyan 2004; Alvarez-Muñiz et al. 2004). Even though GRBs are among the most plausible candidates to accelerate cosmic rays up to ultra-high energies ( $\gtrsim 10^{18} \text{ eV}$ ; Waxman 1995; Vietri 1995) and thus, potential candidates for neutrino detection, the IceCube collaboration reported no coincidences between neutrinos and GRBs after analyzing years of data (Abbasi et al. 2022, 2012; Aartsen et al. 2016, 2015). Because of this, we rule out hadronic models as an explanation for the observed properties of GRBs and conclude that the number of hadrons is too small for hadronic interactions to efficiently generate observable gamma-ray signals in GRBs. On the other hand, a few bursts GRB 160821B, GRB 180720B, GRB 190114C, GRB 190829A, GRB 201216C and GRB 221009A have been detected, up to now, with photons above  $100 \text{ GeV}$  by the Major Atmospheric Gamma Imaging Cherenkov Telescopes (MAGIC; Acciari et al. 2019; Acciari et al. 2021), the High Energy Stereoscopic System (H.E.S.S.; Abdalla et al. 2019; H. E. S. S. Collaboration 2021) and the Large High-Altitude Air Shower Observatory (LHAASO; LHAASO Collaboration 2023). The VHE emission in all these bursts has been successfully described via SSC FS model (e.g., see Acciari et al. 2021; Abdalla et al. 2019; H. E. S. S. Collaboration 2021; LHAASO Collaboration 2023). Therefore, the most appropriate mechanism to explain the photons above  $10 \text{ GeV}$  in our representative sample is SSC mechanism from FSs. It should be noted that the values of the spectral breaks derived from the best-fit parameters (see Tables A5 and A6) indicate that the KN effects cannot be neglected in some GRBs of our sample. Based on the maximum photon energy emitted by synchrotron radiation during the deceleration phase, several authors have claimed that some LAT light curves cannot be adequately interpreted in terms of only synchrotron FS radiation (Ghisellini et al. 2010; Maxham et al. 2011; Fraija 2015; Fraija et al. 2016a, 2020). Therefore, although the closure relations of the synchrotron standard model could satisfy the 29 LAT-detected GRBs with VHE emission above  $10 \text{ GeV}$  reported in the 2FLGC, this model is not the appropriate one, and a new mechanism such as SSC would be the better favored as shown in this manuscript.

## 4 SUMMARY

Based on the external FS scenario in the stellar wind and homogeneous medium, we have presented a general analytical model of the synchrotron and SSC processes in the fully adiabatic ( $\epsilon = 0$ ), fully radiative ( $\epsilon = 1$ ) or partially radiative or adiabatic ( $0 < \epsilon < 1$ ) regimes for an electron spectral index in the ranges of  $1 < p < 2$  and  $2 \leq p$ . Using the typical values of a GRB afterglow and assuming that all electrons are accelerated during the FS, we explicitly derived and plotted the expected synchrotron and SSC light curves and spectra in the stellar-wind and constant-density medium for each range of  $p$ . We calculated the spectral breaks in the KN regime (Nakar et al. 2009; Wang et al. 2010) and introduced the effect of EBL absorption as proposed in Franceschini & Rodighiero (2017). We discuss the evolution of the SSC flux as a function of the equivalent kinetic energy, density parameter, electron spectral index, and radiative parameter. We compared the expected SSC fluxes with the CTA, MAGIC, and *Fermi*/LAT sensitivities (Fioretti et al. 2019). We showed that all the expected fluxes are below the *Fermi*/LAT sensitivity, and depending on the parameter values, they could be detected by the CTA or MAGIC Telescopes. In particular, when  $\epsilon = 0$ , the standard synchrotron and SSC light curves derived in the standard stellar wind and homogeneous medium afterglow models for  $1 < p < 2$  and  $2 \leq p$  are recovered (Sari et al. 1998; Panaitescu & Mészáros 1998; Chevalier & Li 2000; Bhattacharya 2001; Sari & Esin 2001; Gao et al. 2013; Fraija et al. 2019b).

Adiabatic breaks around the transition time between fast- and slow-cooling regimes are expected in the light curves. However, if the value of

$p$  does not deviate from 2, adiabatic breaks are not observed. We have derived the closure relations between the temporal and spectral indices that describe the evolution of the synchrotron and SSC flux as a function of  $\epsilon$  and  $p$ . Significant variations of the spectral and temporal features of the afterglow emission are introduced by radiative losses only if  $\epsilon$  is large and approaches to unity. Otherwise, Deviations around  $\epsilon = 0$  will produce small variations of the spectral and temporal features. In the fully adiabatic regime, the temporal evolution of the synchrotron flux in the stellar wind and constant-density medium is identical. On the contrary, in the radiative regime, they evolve differently in both density profiles. Therefore, an afterglow transition between stellar wind and homogeneous medium would be easily identifiable in the radiative regime.

Given the closure relations (see Table A1), we notice that synchrotron and SSC fluxes could have a similar evolution in time and energy when condition  $\alpha_{\text{syn}}(\beta) \approx \alpha_{\text{SSC}}(\beta)$  is satisfied. For a stellar wind and constant density medium, the condition is reached when  $\beta \rightarrow 1$  and the observed frequency evolves under the cooling condition of  $\{\nu_m^j, \nu_c^j\} < \nu$  with  $j = \text{ssc}$  and  $\text{syn}$ . Irrespective of the value of  $p$ , the temporal decay indices become  $\alpha \approx \frac{4}{4-\epsilon}$  and  $\approx \frac{2(4+\epsilon)}{8-\epsilon}$  for a wind and homogeneous medium, respectively. Temporal and spectral similarities observed in two different bands of afterglow emission (e.g., TeV gamma-rays, X-rays and optical bands) could be explained through the synchrotron and SSC FS model with a hard electron spectral index  $p \approx 2$ . If  $\epsilon \approx 0$ , the expected flux in the stellar wind or constant-density medium evolves with a temporal index of  $\alpha \approx 1$ , the parameter  $\epsilon$  could be used to discriminate between the afterglow models. It can be seen in Table A1 that the closure relations of the synchrotron and SSC models with  $\epsilon \approx 1$ , and the cooling condition  $\{\nu_m^k, \nu_c^k\} < \nu$  (with  $k = \text{syn}$  and  $\text{ssc}$ ) favor the powerful LAT-detected GRBs described with  $\beta \sim 1$  and  $\alpha \sim 1.5$  as reported by Ghisellini et al. (2010). GRBs described with  $\alpha > 2$  and  $\beta < 1$  satisfied the closure relations of the SSC model under the cooling condition  $\nu_m^{\text{SSC}} < \nu < \nu_c^{\text{SSC}}$  with  $0 \leq \epsilon \leq 1$ , which is difficult to explain with the standard synchrotron model. GRBs satisfy the synchrotron closure relations of a homogeneous medium of a cooling condition  $\nu_m^{\text{syn}} < \nu < \nu_c^{\text{syn}}$  for  $\epsilon = 0$  or a cooling condition of  $\{\nu_m^{\text{syn}}, \nu_c^{\text{syn}}\} < \nu$  for  $\epsilon = 1$ . For example, given a value of  $p = 2.8$  and a cooling condition of  $\nu_m^{\text{syn}} < \nu < \nu_c^{\text{syn}}$ , the corresponding spectral and temporal indices are  $\beta = 0.9$  and  $\alpha = 1.35$ , respectively. A similar result could be obtained considering a value of  $p = 1.8$  and a cooling condition of  $\{\nu_m^{\text{syn}}, \nu_c^{\text{syn}}\} < \nu$  with  $\epsilon = 0.92$ . It is worth noting that if  $h\nu \approx 100$  MeV, the first condition  $\nu_m^{\text{syn}} < \nu < \nu_c^{\text{syn}}$  might require (due to  $\nu_c^{\text{syn}} \propto \epsilon_B^{-\frac{3}{2}}$ ) an atypical value of the magnetic microphysical parameter (e.g.  $\epsilon_B \lesssim 10^{-6}$ ; Kumar & Barniol Duran 2009, 2010) whereas the second one leads to an usual value of the microphysical parameter (e.g.,  $3 \times 10^{-5} \lesssim \epsilon_B \lesssim 0.3$ ; Santana et al. 2014).

As particular cases, we have derived the *Fermi*/LAT light curves together with the photons with energies  $\geq 100$  MeV associated with each burst. We have selected those GRBs (080825C, 090510, 090902B, 090926A, 110731A, 130502B, 141207A, 170214A and 180720B) from the 2FLGC (Ajello et al. 2019b) with values of temporal and spectral indices with  $\alpha_L \gtrsim 1.5$  and  $\Gamma_L \approx 2$ , respectively. We have applied our adiabatic-radiative afterglow model to fit the observations of this sample. We want to highlight that the standard SSC or synchrotron afterglow model cannot describe the closure relations of GRBs with both the temporal decay index  $\alpha_L \gtrsim 1.5$  and the spectral index  $\Gamma_L \approx 2$ . It is always possible to assume light curves from synchrotron and SSC models to superimpose them and describe some temporal evolution different from that predicted by the standard afterglow model. However, light curves in the radiative regime can be done in an evident and clean way. We have used the multiwavelength observations to constrain the parameters in the synchrotron and SSC mechanism and model the LAT light curves of the sample via MCMC simulations. We have fitted the LAT observations of GRB 080825C, GRB 130502B and GRB 141207A with the FS model evolving in the stellar-wind and constant-density environment, the LAT, X-ray and optical observations of GRB 090510, GRB 090926A and GRB 170214 using the constant-density medium, and GRB 090902B, GRB 110731A and GRB 180720B with the stellar-wind environment. The results indicate that although the fraction of the total energy density given to accelerate electrons is much greater than  $\epsilon_e \gg 0.1$ , the shock-accelerated electrons are not in the fast-cooling regime during the entire LAT light curve. This indicates that in some cases a transition from radiative to adiabatic regime occurs in the LAT observations.

## ACKNOWLEDGEMENTS

We would like to extend our appreciation to the anonymous referee for their thorough evaluation of the article and valuable suggestions, which significantly improved the quality and clarity of our manuscript. We also thank Tanmoy Laskar, Paz Beniamini and Bin Zhang for useful discussions. NF acknowledges financial support from UNAM-DGAPA-PAPIIT through grants IN106521 and IN119123. PV acknowledges financial support from NASA grants 80NSSC19K0595 and NNM11AA01A.

## DATA AVAILABILITY

No new data were generated or analysed in support of this research.

## REFERENCES

- Aartsen M. G., et al., 2015, *ApJ*, 805, L5  
 Aartsen M. G., et al., 2016, *ApJ*, 824, 115  
 Abbasi R., et al., 2012, *Nature*, 484, 351

- Abbasi R., et al., 2022, arXiv e-prints, [p. arXiv:2205.11410](https://arxiv.org/abs/2205.11410)
- Abbott B. P., Abbott R., Abbott T. D., Acernese F., Ackley K., LIGO Scientific Collaboration Virgo Collaboration 2017a, *Phys. Rev. Lett.*, **119**, 161101
- Abbott B. P., et al., 2017b, *ApJ*, **848**, L13
- Abdalla H., et al., 2019, *Nature*, **575**, 464
- Abdo A. A., et al., 2009a, *ApJ*, **706**, L138
- Abdo A. A., et al., 2009b, *ApJ*, **707**, 580
- Abdollahi S., et al., 2022, *ApJS*, **260**, 53
- Acciari V. A., Ansoldi S., Antonelli L. A., Engels A. A., et al. 2019, *Nature*, **575**, 459
- Acciari V. A., Ansoldi S., Antonelli L. A., Arbet Engels A., Asano K., et al. 2021, *ApJ*, **908**, 90
- Ackermann M., et al. 2010, *ApJ*, **716**, 1178
- Ackermann M., et al., 2011, *ApJ*, **729**, 114
- Ackermann M., et al., 2013, *ApJ*, **763**, 71
- Ackermann M., et al., 2014, *Science*, **343**, 42
- Ajello M., Arimoto M., Axelsson M., Baldini L., Barbiellini G., et al. 2019a, *ApJ*, **878**, 52
- Ajello M., et al., 2019b, *ApJ*, **878**, 52
- Ajello M., et al., 2019c, *ApJ*, **886**, L33
- Alvarez-Muñiz J., Halzen F., Hooper D., 2004, *ApJ*, **604**, L85
- Amaral-Rogers A., Evans P. A., 2014, GRB Coordinates Network, [17149](https://www.gcn.org/coordinates/2014/01/17149.html), 1
- Arimoto M., Kocevski D., Desiante R., Axelsson M., 2014, GRB Coordinates Network, [17146](https://www.gcn.org/coordinates/2014/01/17146.html), 1
- Asano K., Guiriec S., Mészáros P., 2009, *ApJ*, **705**, L191
- Band D., et al., 1993, *ApJ*, **413**, 281
- Barthelmy S. D., et al., 2018, GRB Coordinates Network, [22998](https://www.gcn.org/coordinates/2018/01/22998.html), 1
- Beardmore A. P., et al., 2017, GRB Coordinates Network, [20691](https://www.gcn.org/coordinates/2017/01/20691.html), 1
- Becerra R. L., et al., 2017, *ApJ*, **837**, 116
- Becerra R. L., et al., 2019, *ApJ*, **887**, 254
- Berger E., 2014, *ARA&A*, **52**, 43
- Bersier D., 2011, GRB Coordinates Network, [12216](https://www.gcn.org/coordinates/2011/01/12216.html), 1
- Bhattacharya D., 2001, Bulletin of the Astronomical Society of India, **29**, 107
- Bissaldi E., 2009, GRB Coordinates Network, [9933](https://www.gcn.org/coordinates/2009/01/9933.html), 1
- Bissaldi E., Racusin J. L., 2018, GRB Coordinates Network, Circular Service, No. 22980, #1 (2018), [22980](https://www.gcn.org/coordinates/2018/01/22980.html)
- Blandford R. D., McKee C. F., 1976, *Physics of Fluids*, **19**, 1130
- Bloom J. S., Frail D. A., Sari R., 2001, *AJ*, **121**, 2879
- Böttcher M., Dermer C. D., 2000, *ApJ*, **532**, 281
- Bouvier A., et al., 2008, GRB Coordinates Network, [8183](https://www.gcn.org/coordinates/2008/01/8183.html), 1
- Breeveld A. A., Immler S., 2013, GRB Coordinates Network, [14544](https://www.gcn.org/coordinates/2013/01/14544.html), 1
- Burns E., 2014, GRB Coordinates Network, [17150](https://www.gcn.org/coordinates/2014/01/17150.html), 1
- Cavallo G., Rees M. J., 1978, *MNRAS*, **183**, 359
- enko S. B., et al., 2011, *ApJ*, **732**, 29
- enko S. B., Perley D. A., Singer L. P., 2013, GRB Coordinates Network, [14541](https://www.gcn.org/coordinates/2013/01/14541.html), 1
- Chakrabarti S. K., et al., 2009, GRB Coordinates Network, Circular Service, No. 109, #1 (2009), [10009](https://www.gcn.org/coordinates/2009/01/10009.html)
- Chevalier R. A., Li Z.-Y., 2000, *ApJ*, **536**, 195
- Corsi A., enko S. B., Perley D. A., 2013, GRB Coordinates Network, [15502](https://www.gcn.org/coordinates/2013/01/15502.html), 1
- Cucchiara A., Fox D. B., Tanvir N., Berger E., 2009, GRB Coordinates Network, [9873](https://www.gcn.org/coordinates/2009/01/9873.html)
- Dai Z. G., Cheng K. S., 2001, *ApJ*, **558**, L109
- Dai Z. G., Lu T., 1998, *MNRAS*, **298**, 87
- De Pasquale M., et al., 2010, *ApJ*, **709**, L146
- Dermer C. D., Atoyan A., 2004, *A&A*, **418**, L5
- Dermer C. D., Böttcher M., Chiang J., 2000, *ApJ*, **537**, 255
- Evans P. A., 2018, GRB Coordinates Network, Circular Service, No. 22986, #1 (2018), [22986](https://www.gcn.org/coordinates/2018/01/22986.html)
- Evans P. A., Willingale R., Osborne J. P., O'Brien P. T., Page K. L., et al. 2010, *A&A*, **519**, A102
- Fioretti V., Ribeiro D., Humensky T. B., Bulgarelli A., Maier G., Moralejo A., Nigro C., 2019, in 36th International Cosmic Ray Conference (ICRC2019). p. 673 ([arXiv:1907.08018](https://arxiv.org/abs/1907.08018))
- Fraija N., 2015, *ApJ*, **804**, 105
- Fraija N., Veres P., 2018, *ApJ*, **859**, 70
- Fraija N., González M. M., Lee W. H., 2012, *ApJ*, **751**, 33
- Fraija N., Lee W., Veres P., 2016a, *ApJ*, **818**, 190
- Fraija N., Lee W. H., Veres P., Barniol Duran R., 2016b, *ApJ*, **831**, 22
- Fraija N., et al., 2017, *ApJ*, **848**, 15
- Fraija N., Dichiarà S., Pedreira A. C. C. d. E. S., Galvan-Gamez A., Becerra R. L., Barniol Duran R., Zhang B. B., 2019a, *ApJ*, **879**, L26
- Fraija N., Barniol Duran R., Dichiarà S., Beniamini P., 2019b, *ApJ*, **883**, 162
- Fraija N., et al., 2019c, *ApJ*, **885**, 29
- Fraija N., et al., 2019d, *ApJ*, **885**, 29
- Fraija N., Laskar T., Dichiarà S., Beniamini P., Duran R. B., Dainotti M. G., Becerra R. L., 2020, *ApJ*, **905**, 112
- Fraija N., Dainotti M. G., Ugale S., Jyoti D., Warren D. C., 2022a, *ApJ*, **934**, 188
- Fraija N., Galvan-Gamez A., Betancourt Kamenetskaia B., Dainotti M. G., Dichiarà S., Veres P., Becerra R. L., do E. S. Pedreira A. C. C., 2022b, *ApJ*, **940**, 189
- Fraija N., Dainotti M. G., Levine D., Kamenetskaia B. B., Galvan-Gamez A., 2023, *ApJ*, **958**, 126
- Fraija N., Dainotti M. G., Betancourt Kamenetskaia B., Galván-Gómez A., Aguilar-Ruiz E., 2024, *MNRAS*, **527**, 1884
- Franceschini A., Rodighiero G., 2017, *A&A*, **603**, A34



- Gao H., Lei W.-H., Zou Y.-C., Wu X.-F., Zhang B., 2013, *New Astronomy Reviews*, 57, 141
- Ghisellini G., Ghirlanda G., Nava L., Celotti A., 2010, *MNRAS*, 403, 926
- Giuliani A., et al., 2014, *arXiv e-prints*, p. arXiv:1407.0238
- Goldstein A., et al., 2017, *ApJ*, 848, L14
- Golenetskii S., et al., 2009, GRB Coordinates Network, 9959, 1
- Golenetskii S., et al., 2011, GRB Coordinates Network, 12223, 1
- Gruber D., 2011, GRB Coordinates Network, 12221, 1
- Guetta D., Spada M., Waxman E., 2001, *ApJ*, 557, 399
- H. E. S. S. Collaboration 2021, *arXiv e-prints*, p. arXiv:2106.02510
- Hanabata Y., et al., 2011, GRB Coordinates Network, 12244, 1
- Kennea J. A., Stratta G., 2009, GRB Coordinates Network, 9868
- Kobayashi S., Zhang B., Mészáros P., Burrows D., 2007, *ApJ*, 655, 391
- Kocevski D., Vianello G., Chiang J., Racusin J., 2013, GRB Coordinates Network, 14532, 1
- Kouveliotou C., Meegan C. A., Fishman G. J., Bhat N. P., Briggs M. S., Koshut T. M., Paciesas W. S., Pendleton G. N., 1993, *ApJ*, 413, L101
- Kruehler T., Schady P., Greiner J., Tanvir N. R., 2017, GRB Coordinates Network, 20686, 1
- Kumar P., Barniol Duran R., 2009, *MNRAS*, 400, L75
- Kumar P., Barniol Duran R., 2010, *MNRAS*, 409, 226
- Kumar P., Panaitescu A., 2008, *MNRAS*, 391, L19
- Kumar P., Zhang B., 2015, *Phys. Rep.*, 561, 1
- LHAASO Collaboration 2023, *arXiv e-prints*, p. arXiv:2306.06372
- Li Z., Dai Z. G., Lu T., 2002, *MNRAS*, 330, 955
- Mailyan B., Meegan C., 2017, GRB Coordinates Network, 20675, 1
- Malesani D., et al., 2009, GRB Coordinates Network, 9942, 1
- Malesani D., Leloudas G., Xu D., de Ugarte Postigo A., Hjorth J., Jakobsson P., Nielsen M. B., 2011, GRB Coordinates Network, 12220, 1
- Maxham A., Zhang B.-B., Zhang B., 2011, *MNRAS*, 415, 77
- Mazaeva E., Pozanenko A., Klunko E., Volnova A., 2017, GRB Coordinates Network, 20687, 1
- Melandri A., Immler S., 2013, GRB Coordinates Network, 14540, 1
- Mészáros P., Rees M. J., 2000, *ApJ*, 541, L5
- Moderski R., Sikora M., Bulik T., 2000, *ApJ*, 529, 151
- Moretti E., Axelsson M., 2016, *MNRAS*, 458, 1728
- Moskvitin A. S., Sokolov V. V., Spiridonova O. I., Andreev M. V., Sergeev A. V., Parakhin N. A., 2011, GRB Coordinates Network, 12333, 1
- Nakar E., Ando S., Sari R., 2009, *ApJ*, 703, 675
- Nappo F., Ghisellini G., Ghirlanda G., Melandri A., Nava L., Burlon D., 2014, *MNRAS*, 445, 1625
- Nicuesa Guelbenzu A., et al., 2012, *A&A*, 538, L7
- Noda K., et al., 2009, GRB Coordinates Network, 9951
- Oates S. R., et al., 2011, GRB Coordinates Network, 12215, 1
- Panaitescu A., 2005, *MNRAS*, 362, 921
- Panaitescu A., 2019, *ApJ*, 886, 106
- Panaitescu A., Kumar P., 2002, *ApJ*, 571, 779
- Panaitescu A., Mészáros P., 1998, *ApJ*, 501, 772
- Pandey S. B., et al., 2010, *ApJ*, 714, 799
- Pereyra M., et al., 2022, *MNRAS*, 511, 6205
- Perley D. A., et al., 2014, *ApJ*, 781, 37
- Petropoulou M., Piran T., Mastichiadis A., 2015, *MNRAS*, 452, 3226
- Piran T., 1999, *Phys. Rep.*, 314, 575
- Piran T., Nakar E., 2010, *ApJ*, 718, L63
- Planck Collaboration Aghanim N., Akrami Y., Ashdown M., Aumont J., Baccigalupi C., Ballardini M., Banday A. J. e. a., 2018, *arXiv e-prints*, p. arXiv:1807.06209
- Racusin J. L., Karpov S. V., Sokolowski M., Granot J., Wu X. F., et al. 2008, *Nature*, 455, 183
- Racusin J. L., et al., 2009, *ApJ*, 698, 43
- Racusin J. L., Vianello G., Perkins J., 2017, GRB Coordinates Network, 20676, 1
- Rau A., McBreen S., Kruehler T., 2009, GRB Coordinates Network, 9353, 1
- Rau A., et al., 2010, *ApJ*, 720, 862
- Roberts O. J., Meegan C., 2018, GRB Coordinates Network, Circular Service, No. 22981, #1 (2018), 22981
- Rybicki G. B., Lightman A. P., 1986, *Radiative Processes in Astrophysics*
- Santana R., Barniol Duran R., Kumar P., 2014, *ApJ*, 785, 29
- Sari R., Esin A. A., 2001, *ApJ*, 548, 787
- Sari R., Piran T., Narayan R., 1998, *ApJ*, 497, L17
- Sasada M., Nakaoka T., Kawabata M., Uchida N., Yamazaki Y., Kawabata K. S., 2018, GRB Coordinates Network, Circular Service, No. 22977, #1 (2018), 22977
- Soderberg A. M., et al., 2006, *ApJ*, 650, 261
- Stroh M. C., Kennea J. A., 2013, GRB Coordinates Network, 15468, 1
- Swenson C. A., Siegel M. H., 2009, GRB Coordinates Network, 9869
- Swenson C. A., et al., 2010, *ApJ*, 718, L14
- Tak D., Omodei N., Uhm Z. L., Racusin J., Asano K., McEnery J., 2019, *ApJ*, 883, 134
- Tang Q.-W., Wang X.-Y., Liu R.-Y., 2017, *ApJ*, 844, 56
- Tanvir N. R., Wiersema K., Levan A. J., Cenko S. B., Geballe T., 2011, GRB Coordinates Network, 12225, 1
- Tehekovskoy A., McKinney J. C., Narayan R., 2008, *MNRAS*, 388, 551

**Table A1.** Closure relations of the SSC and synchrotron afterglow model in stellar-wind and homogeneous medium with  $j = \text{ssc}$  and  $\text{syn}$ , respectively.

		Synchrotron			SSC	
		$\beta$	$\alpha(\beta)$	$\alpha(\beta)$	$\alpha(\beta)$	$\alpha(\beta)$
			$(1 < p < 2)$	$(2 < p)$	$(1 < p < 2)$	$(2 < p)$
ISM, Slow Cooling						
1	$\nu_m^j < \nu < \nu_c^j$	$\frac{p-1}{2}$	$\frac{3(2\beta+3+2\epsilon)}{2(8-\epsilon)}$	$\frac{3(4\beta+\epsilon)}{8-\epsilon}$	—	$\frac{2(2\epsilon+9\beta-1)}{8-\epsilon}$
2	$\nu_c^j < \nu$	$\frac{p}{2}$	$\frac{3\beta+5+2\epsilon}{8-\epsilon}$	$\frac{2(6\beta+\epsilon-2)}{8-\epsilon}$	—	$\frac{2(\epsilon+9\beta-5)}{8-\epsilon}$
ISM, Fast Cooling						
3	$\nu_c^j < \nu < \nu_m^j$	$\frac{1}{2}$	$\frac{4\beta(\epsilon+1)}{8-\epsilon}$	$\frac{4\beta(\epsilon+1)}{8-\epsilon}$	$\frac{2(2\epsilon-1)\beta}{8-\epsilon}$	$\frac{2(2\epsilon-1)\beta}{8-\epsilon}$
4	$\nu_m^j < \nu$	$\frac{p}{2}$	$\frac{3\beta+5+2\epsilon}{8-\epsilon}$	$\frac{2(6\beta+\epsilon-2)}{8-\epsilon}$	—	$\frac{2(\epsilon+9\beta-5)}{8-\epsilon}$
Wind, Slow Cooling						
5	$\nu_m^j < \nu < \nu_c^j$	$\frac{p-1}{2}$	$\frac{2\beta+9-\epsilon}{2(4-\epsilon)}$	$\frac{2+\beta(6-\epsilon)}{4-\epsilon}$	$\frac{9-2\epsilon+\beta(\epsilon-2)}{4-\epsilon}$	$\frac{4-\epsilon+\beta(8-\epsilon)}{4-\epsilon}$
6	$\nu_c^j < \nu$	$\frac{p}{2}$	$\frac{\beta+3}{4-\epsilon}$	$\frac{\epsilon-2+\beta(6-\epsilon)}{4-\epsilon}$	$\frac{6-\epsilon+\beta(\epsilon-2)}{4-\epsilon}$	$\frac{\epsilon-4+\beta(8-\epsilon)}{4-\epsilon}$
Wind, Fast Cooling						
7	$\nu_c^j < \nu < \nu_m^j$	$\frac{1}{2}$	$\frac{(\epsilon+2)\beta}{4-\epsilon}$	$\frac{(\epsilon+2)\beta}{4-\epsilon}$	$\frac{\epsilon\beta}{4-\epsilon}$	$\frac{\epsilon\beta}{4-\epsilon}$
8	$\nu_m^j < \nu$	$\frac{p}{2}$	$\frac{\beta+3}{4-\epsilon}$	$\frac{\epsilon-2+\beta(6-\epsilon)}{4-\epsilon}$	$\frac{6-\epsilon+\beta(\epsilon-2)}{4-\epsilon}$	$\frac{\epsilon-4+\beta(8-\epsilon)}{4-\epsilon}$

- Tsang O., Kirk J. G., 2007, *A&A*, **463**, 145  
Ukwatta T. N., et al., 2009, GRB Coordinates Network, **9337**, 1  
Veres P., Mészáros P., 2012, *ApJ*, **755**, 12  
Vestrand W. T., et al., 2014, *Science*, **343**, 38  
Vietri M., 1995, *ApJ*, **453**, 883  
Vink J. S., de Koter A., 2005, *A&A*, **442**, 587  
Volnova A., Krugly Y., Inasaridze R., Slyusarev I., Inasaridze G., Zhuzhunadze V., Molotov I., Pozanenko A., 2013a, GRB Coordinates Network, **15484**, 1  
Volnova A., Varda D., Sinyakov E., Molotov I., Pozanenko A., 2013b, GRB Coordinates Network, **15485**, 1  
Vreeswijk P. M., et al., 2018, GRB Coordinates Network, Circular Service, No. 22996, #1 (2018), **22996**  
Wang X.-Y., He H.-N., Li Z., Wu X.-F., Dai Z.-G., 2010, *ApJ*, **712**, 1232  
Waxman E., 1995, *Physical Review Letters*, **75**, 386  
Wijers R. A. M. J., Galama T. J., 1999, *ApJ*, **523**, 177  
Wu X. F., Dai Z. G., Huang Y. F., Lu T., 2005, *ApJ*, **619**, 968  
Yost S. A., Harrison F. A., Sari R., Frail D. A., 2003, *ApJ*, **597**, 459  
Zauderer A., Berger E., Frail D. A., 2011, GRB Coordinates Network, **12227**, 1  
Zhang B., 2019, arXiv e-prints, p. [arXiv:1911.09862](https://arxiv.org/abs/1911.09862)  
Zhang B., et al., 2007, *ApJ*, **655**, 989  
van der Horst A. J., Connaughton V., 2008a, GRB Coordinates Network, Circular Service, No. 8141, (2008), 8141  
van der Horst A. J., Connaughton V., 2008b, GRB Coordinates Network, **8141**, 1  
von Kienlin A., Younes G., 2013, GRB Coordinates Network, **14530**, 1

## APPENDIX A: SOME EXTRA MATERIAL

This paper has been typeset from a  $\text{\LaTeX}$  file prepared by the author.

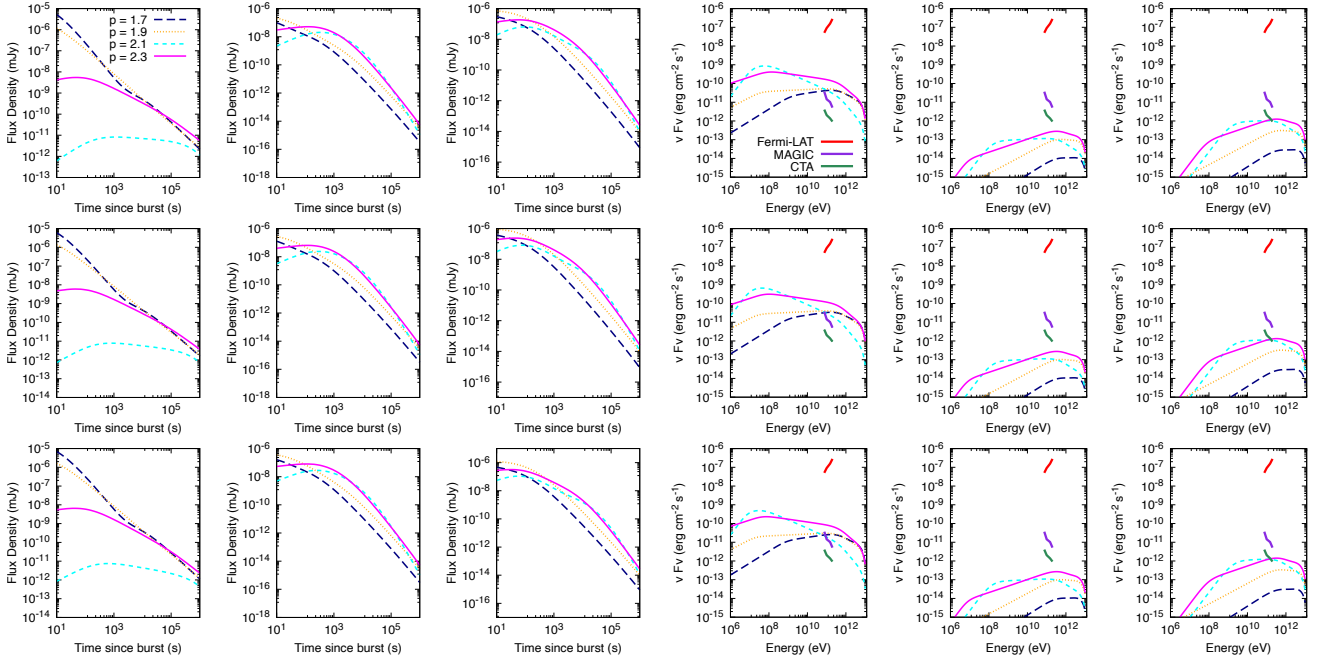


**Figure A1.** SSC light curves (left) and spectra (right) in the stellar-wind afterglow model for  $\epsilon = 0$  (upper panels), 0.2 (center panels) and 0.4 (lower panels) and  $p = 1.7, 1.9, 2.1$  and  $2.3$ . The light curves and SED are shown at 1 TeV and  $5 \times 10^4$  s, respectively, for  $\epsilon_e = 0.1$ ,  $\epsilon_B = 10^{-4}$  and  $\zeta = 0.5$ . The values of parameter pairs ( $A_W = 0.1$  and  $E = 10^{52}$  erg), ( $A_W = 10^{-3}$  and  $E = 10^{52}$  erg), and ( $A_W = 10^{-3}$  and  $E = 10^{53}$  erg) are used for the left, middle and right panels. The sensitivities of CTA (Southern array, green line), MAGIC (purple line) and *Fermi*/LAT (red line) are shown between 75 and 250 GeV at  $3 \times 10^4$  s for a zenith angle of  $20^\circ$  (Fioretti et al. 2019). We have considered a hypothetical burst located at  $z = 0.1$  and the effect of the EBL absorption proposed in (Franceschini & Rodighiero 2017).

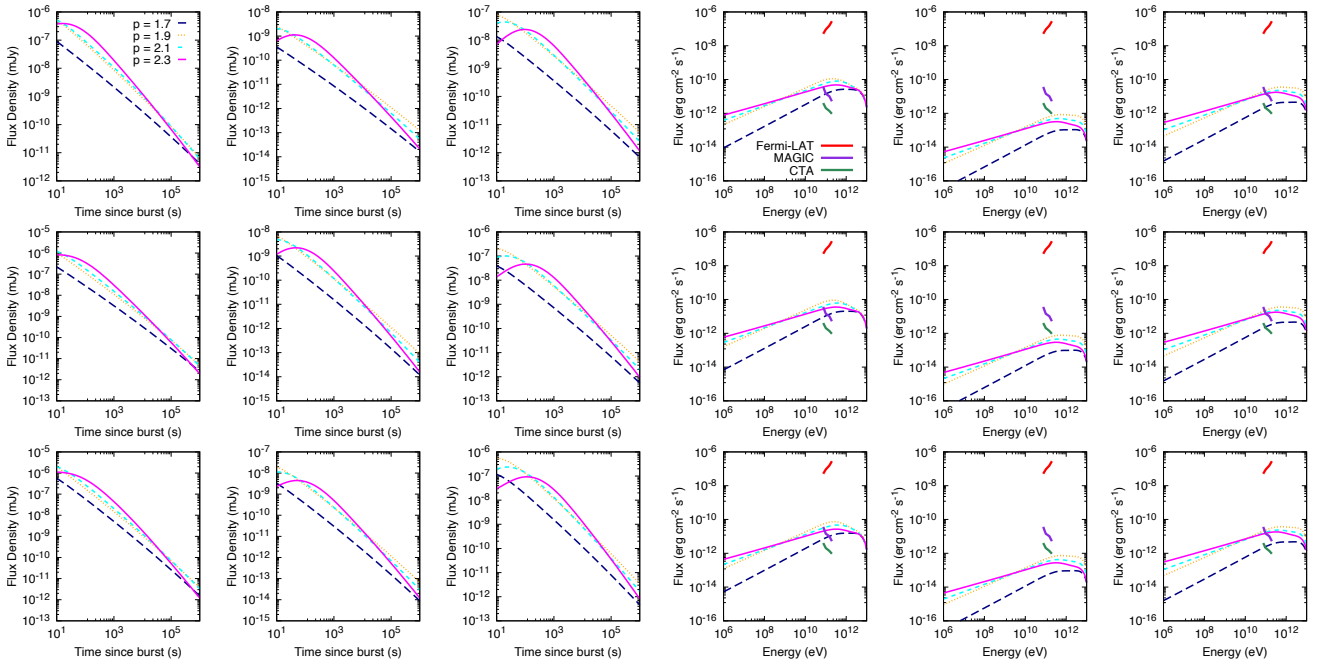


**Figure A2.** The same as Figure A1, but for a constant-density medium. The values of parameter pairs ( $n = 0.1 \text{ cm}^{-3}$  and  $E = 10^{52}$  erg), ( $n = 10^{-3} \text{ cm}^{-3}$  and  $E = 10^{52}$  erg), and ( $n = 10^{-3} \text{ cm}^{-3}$  and  $E = 10^{53}$  erg) are used for the left, middle and right panels.

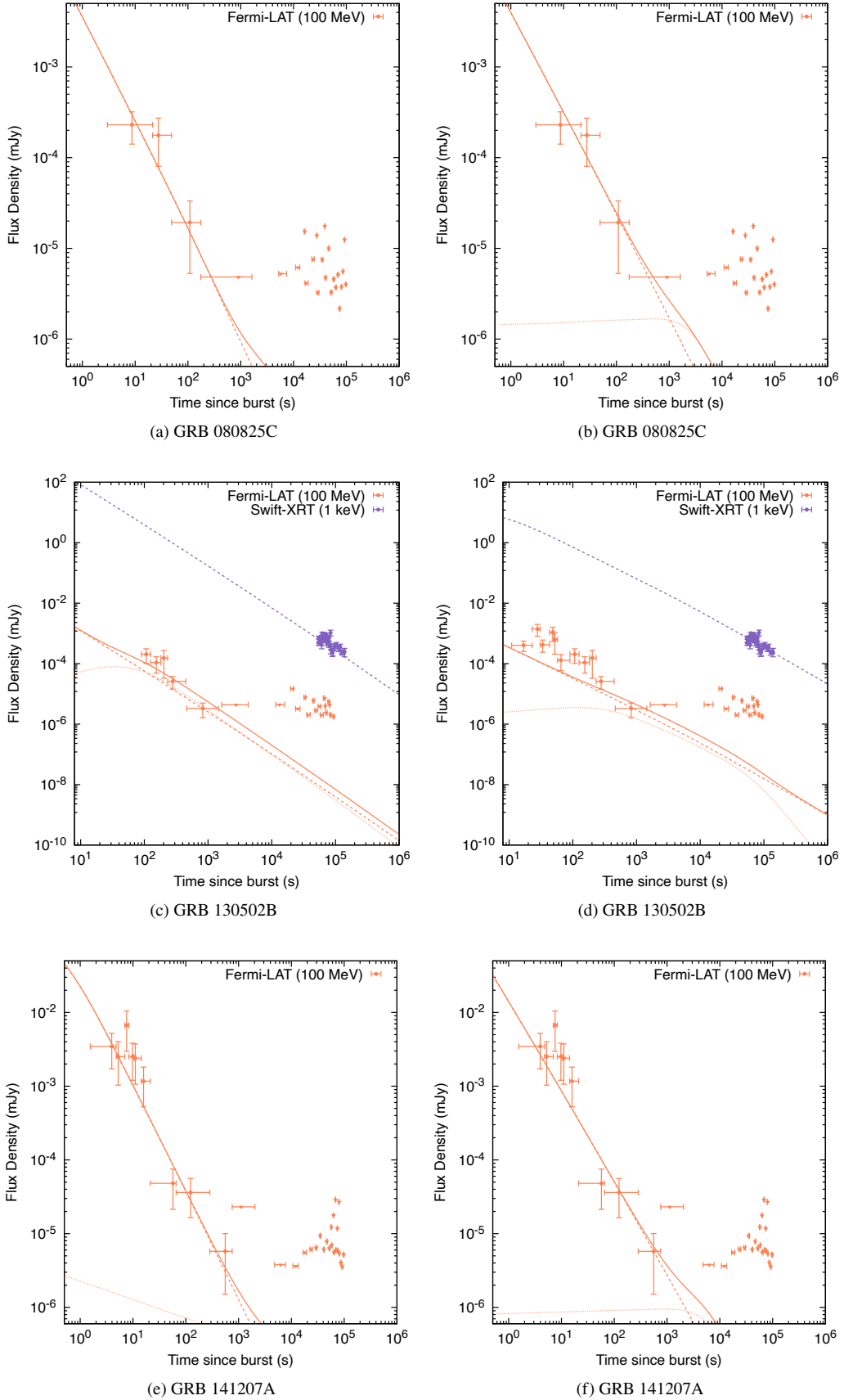


**Figure A3.** The LAT and X-ray observations with the best-fit curves using the FS model evolving in the stellar-wind (right) and homogeneous (left) environment. The dashed and dotted lines correspond to synchrotron and SSC models, respectively.

**Table A2.** Sample of 10 GRBs used here. Temporal and spectral indices are taken from [Ajello et al. \(2019b\)](#) with  $\beta_L = \Gamma_L - 1$ .

GRB	$\alpha_L \pm \delta\alpha_L$	$\beta_L \pm \delta\beta_L$
080825C	$1.45 \pm 0.03$	$1.40 \pm 0.40$
090510	$1.81 \pm 0.08$	$1.15 \pm 0.08$
090902B	$1.63 \pm 0.08$	$0.92 \pm 0.06$
090626A	$1.39 \pm 0.08$	$0.86 \pm 0.07$
110731A	$1.50 \pm 0.10$	$1.00 \pm 0.20$
130502B	$1.44 \pm 0.06$	$1.00 \pm 0.10$
141207A	$1.88 \pm 0.03$	$0.80 \pm 0.30$
170214A	$1.70 \pm 0.30$	$1.30 \pm 0.10$
180720B	$1.90 \pm 0.10$	$1.15 \pm 0.10$

**Table A3.** The best-fit values found with MCMC simulations after describing the multiwavelength afterglow observations with a synchrotron model evolving in a constant circumstellar medium.

GRB Name	$\log_{10}(E/\text{erg})$	$\log_{10}(n/\text{cm}^{-3})$	$\log_{10}(\Gamma)$	$\log_{10}(\epsilon_e)$	$\log_{10}(\epsilon_B)$	p
080825C	$52.92^{+0.10}_{-0.10}$	$-1.01^{+0.10}_{-0.09}$	$2.91^{+0.06}_{-0.06}$	$-0.41^{+0.05}_{-0.05}$	$-4.00^{+0.02}_{-0.02}$	$2.24^{+0.01}_{-0.01}$
090510	$53.98^{+0.10}_{-0.10}$	$-1.70^{+0.09}_{-0.09}$	$2.92^{+0.06}_{-0.07}$	$-0.09^{+0.05}_{-0.05}$	$-4.59^{+0.02}_{-0.03}$	$2.60^{+0.04}_{-0.03}$
090926A	$53.85^{+0.12}_{-0.08}$	$-0.02^{+0.10}_{-0.10}$	$2.00^{+0.07}_{-0.06}$	$-0.51^{+0.05}_{-0.05}$	$-1.02^{+0.02}_{-0.03}$	$2.00^{+0.02}_{-0.01}$
130502B	$52.60^{+0.67}_{-0.69}$	$-1.43^{+0.12}_{-0.09}$	$2.01^{+0.63}_{-0.64}$	$-0.56^{+0.01}_{-0.02}$	$-3.19^{+1.42}_{-1.20}$	$2.00^{+0.02}_{-0.01}$
141207A	$52.95^{+0.07}_{-0.10}$	$-1.45^{+0.11}_{-0.10}$	$2.45^{+0.07}_{-0.06}$	$-0.07^{+0.05}_{-0.04}$	$-2.82^{+0.03}_{-0.02}$	$2.55^{+0.10}_{-0.11}$
170214A	$53.97^{+0.10}_{-0.08}$	$-1.00^{+0.10}_{-0.11}$	$2.99^{+0.05}_{-0.06}$	$-0.39^{+0.04}_{-0.05}$	$-4.41^{+0.02}_{-0.02}$	$2.39^{+0.01}_{-0.02}$

**Table A4.** The best-fit values found with MCMC simulations after describing the multiwavelength afterglow observations with a synchrotron model evolving in a stellar-wind environment.

GRB Name	$\log_{10}(E/\text{erg})$	$\log_{10}(A_w)$	$\log_{10}(\Gamma)$	$\log_{10}(\epsilon_e)$	$\log_{10}(\epsilon_B)$	p
080825C	$52.64^{+0.92}_{-1.55}$	$-1.06^{+0.83}_{-0.93}$	$2.51^{+0.33}_{-0.34}$	$-0.26^{+0.13}_{-0.53}$	$-2.13^{+1.05}_{-2.24}$	$2.53^{+0.31}_{-0.51}$
090902B	$54.12^{+0.01}_{-0.01}$	$-2.05^{+0.01}_{-0.01}$	$2.10^{+0.01}_{-0.02}$	$-0.34^{+0.01}_{-0.01}$	$-2.20^{+0.02}_{-0.01}$	$2.02^{+0.02}_{-0.01}$
110731A	$53.95^{+0.47}_{-0.50}$	$-1.47^{+0.43}_{-0.52}$	$2.03^{+0.39}_{-0.55}$	$-0.52^{+0.45}_{-0.42}$	$-2.98^{+0.38}_{-0.55}$	$2.02^{+0.11}_{-0.07}$
130502B	$52.69^{+0.52}_{-0.51}$	$0.01^{+0.53}_{-0.51}$	$2.99^{+0.50}_{-0.48}$	$-0.55^{+0.49}_{-0.45}$	$-4.98^{+0.52}_{-0.51}$	$2.21^{+0.09}_{-0.10}$
141207A	$52.91^{+0.54}_{-0.51}$	$-1.33^{+0.55}_{-0.48}$	$2.51^{+0.50}_{-0.50}$	$-0.06^{+0.56}_{-0.46}$	$-3.27^{+0.47}_{-0.51}$	$2.18^{+0.11}_{-0.08}$
180720B	$53.59^{+0.43}_{-0.52}$	$-3.01^{+0.56}_{-0.49}$	$2.40^{+0.05}_{-0.05}$	$-0.07^{+0.05}_{-0.05}$	$-1.30^{+0.04}_{-0.05}$	$2.03^{+0.02}_{-0.01}$

**Table A5.** Derived quantities at 40 s from the best-fit parameter values found with MCMC simulations with an afterglow model evolving in a homogeneous medium.

GRB	080825C	090510	090926A	130502B	141207A	170214A
$B$ (G)	$2.9 \times 10^{-1}$	$1.4 \times 10^{-1}$	$4.6 \times 10$	$5.1 \times 10^{-1}$	$8.6 \times 10^{-1}$	$3.9 \times 10^{-1}$
$\gamma_m$	$3.3 \times 10^4$	$2.8 \times 10^5$	$2.1 \times 10^3$	$4.6 \times 10^2$	$1.7 \times 10^5$	$1.1 \times 10^5$
$\gamma_c$	$1.7 \times 10^4$	$2.1 \times 10^4$	$3.3 \times 10^1$	$1.5 \times 10^4$	$3.9 \times 10^3$	$8.5 \times 10^3$
$h\nu_m^{\text{syn}}$ (eV)	$6.1 \times 10$	$2.8 \times 10^3$	$2.3 \times 10^1$	$2.4 \times 10^{-2}$	$6.1 \times 10^3$	$5.9 \times 10^2$
$h\nu_c^{\text{syn}}$ (eV)	$1.7 \times 10$	$1.5 \times 10$	$5.5 \times 10^{-3}$	$2.4 \times 10^1$	3.4	3.8
$F_{\text{max}}^{\text{syn}}$ (mJy)	$1.7 \times 10^{-1}$	$2.5 \times 10^{-2}$	$5.6 \times 10^{-2}$	$7.9 \times 10^{-2}$	$2.1 \times 10^{-1}$	$9.8 \times 10^{-3}$
$h\nu_m^{\text{ssc}}$ (GeV)	$6.6 \times 10$	$2.2 \times 10^5$	$1.0 \times 10^{-1}$	$4.9 \times 10^{-6}$	$1.7 \times 10^5$	$6.6 \times 10^3$
$h\nu_c^{\text{ssc}}$ (GeV)	5.1	6.2	$5.9 \times 10^{-9}$	5.2	$5.2 \times 10^{-2}$	$2.8 \times 10^{-1}$
$F_{\text{max}}^{\text{ssc}}$ (mJy)	$3.2 \times 10^{-10}$	$2.6 \times 10^{-11}$	$1.3 \times 10^{-9}$	$9.4 \times 10^{-11}$	$3.2 \times 10^{-10}$	$1.9 \times 10^{-11}$
$h\nu_{\text{KN,m}}^{\text{ssc}}$ (GeV)	$3.6 \times 10^3$	$3.8 \times 10^4$	$1.3 \times 10^2$	$5.6 \times 10^1$	$2.3 \times 10^4$	$8.0 \times 10^3$
$h\nu_{\text{KN,c}}^{\text{ssc}}$ (GeV)	$1.9 \times 10^3$	$2.8 \times 10^3$	2.1	$1.8 \times 10^3$	$5.5 \times 10^2$	$6.4 \times 10^2$

**Table A6.** The same as Table A5, but for an afterglow model evolving in a stellar-wind medium.

GRB	080825C	090902B	110731A	130502B	141207A	180720B
$B$ (G)	$1.9 \times 10$	2.0	3.2	4.7	2.8	$8.5 \times 10^{-1}$
$\gamma_m$	$4.6 \times 10^4$	$8.1 \times 10^3$	$1.0 \times 10^3$	$6.1 \times 10^3$	$4.4 \times 10^4$	$5.5 \times 10^4$
$\gamma_c$	$4.9 \times 10^1$	$1.6 \times 10^3$	$6.5 \times 10^2$	$8.6 \times 10^1$	$3.8 \times 10^2$	$7.9 \times 10^3$
$h\nu_m^{\text{syn}}$ (eV)	$4.3 \times 10^3$	$4.0 \times 10^1$	$5.0 \times 10^{-1}$	9.7	$7.9 \times 10^2$	$1.7 \times 10^3$
$h\nu_c^{\text{syn}}$ (eV)	$4.9 \times 10^{-3}$	1.7	$2.0 \times 10^{-1}$	$2.0 \times 10^{-3}$	$6.0 \times 10^{-2}$	$3.5 \times 10$
$F_{\text{max}}^{\text{syn}}$ (mJy)	2.9	$4.3 \times 10^{-2}$	$8.2 \times 10^{-2}$	$3.2 \times 10$	2.1	$1.1 \times 10^{-2}$
$h\nu_m^{\text{ssc}}$ (GeV)	$9.0 \times 10^3$	2.6	$5.2 \times 10^{-4}$	$3.6 \times 10^{-1}$	$1.5 \times 10^3$	$5.3 \times 10^3$
$h\nu_c^{\text{ssc}}$ (GeV)	$1.2 \times 10^{-8}$	$4.5 \times 10^{-3}$	$8.5 \times 10^{-5}$	$1.4 \times 10^{-8}$	$8.8 \times 10^{-6}$	2.2
$F_{\text{max}}^{\text{ssc}}$ (mJy)	$4.6 \times 10^{-7}$	$3.2 \times 10^{-11}$	$7.7 \times 10^{-10}$	$2.2 \times 10^{-4}$	$9.7 \times 10^{-8}$	$3.2 \times 10^{-13}$
$h\nu_{\text{KN,m}}^{\text{ssc}}$ (GeV)	$2.7 \times 10^3$	$1.4 \times 10^3$	$8.4 \times 10$	$1.9 \times 10^2$	$3.6 \times 10^3$	$2.1 \times 10^4$
$h\nu_{\text{KN,c}}^{\text{ssc}}$ (GeV)	2.9	$2.9 \times 10^2$	$5.3 \times 10$	2.6	3.1	$3.0 \times 10^3$

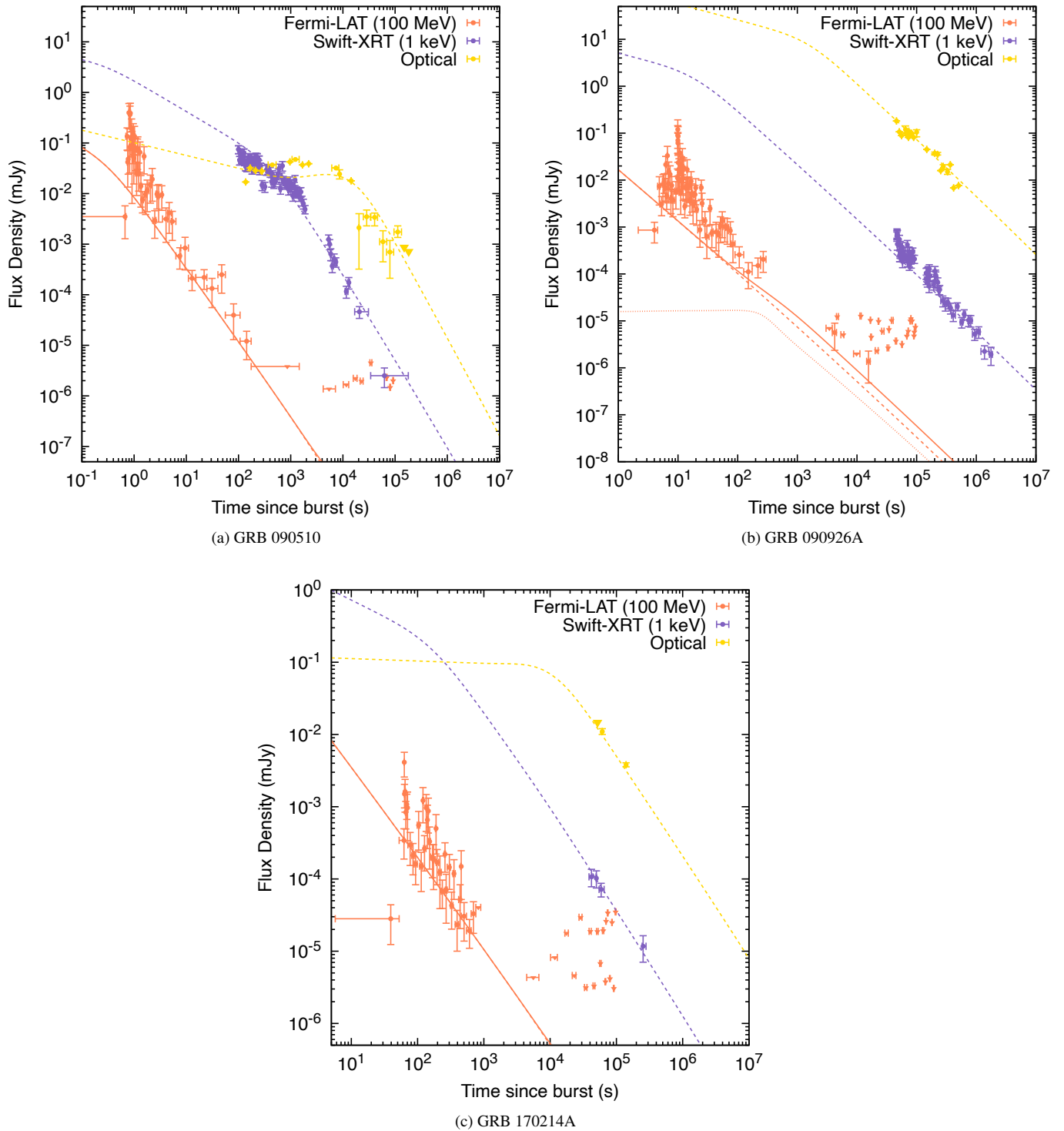


**Figure A4.** The LAT (peach), X-ray (purple) and optical (yellow) observations with the best-fit curves using the forward-shock model evolving in the homogeneous medium. The dashed and dotted lines correspond to synchrotron and SSC models, respectively.

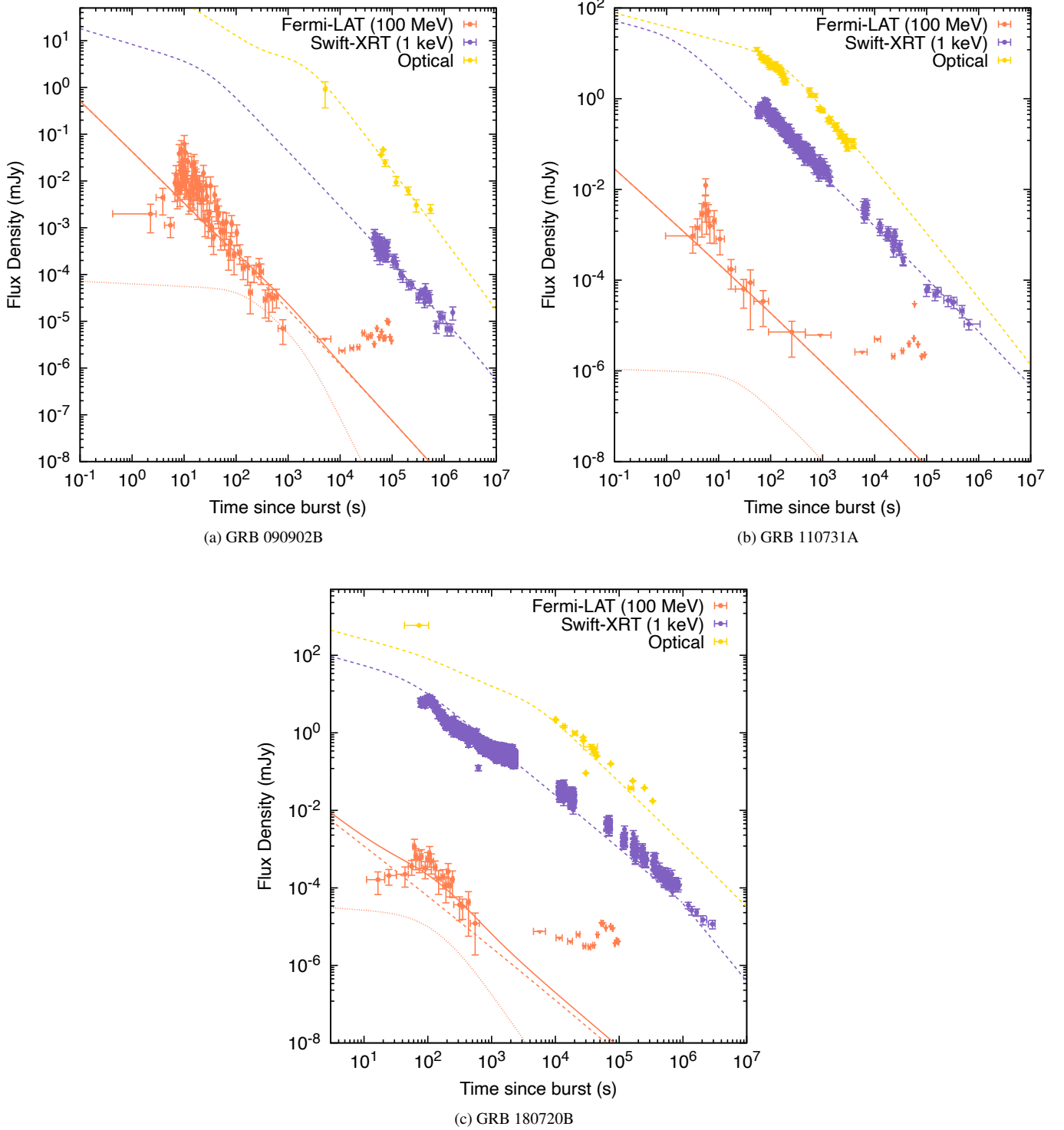


**Figure A5.** The LAT, X-ray and optical observations with the best-fit curves using the FS model evolving in stellar-wind environment. The dashed and dotted lines correspond to synchrotron and SSC models, respectively.



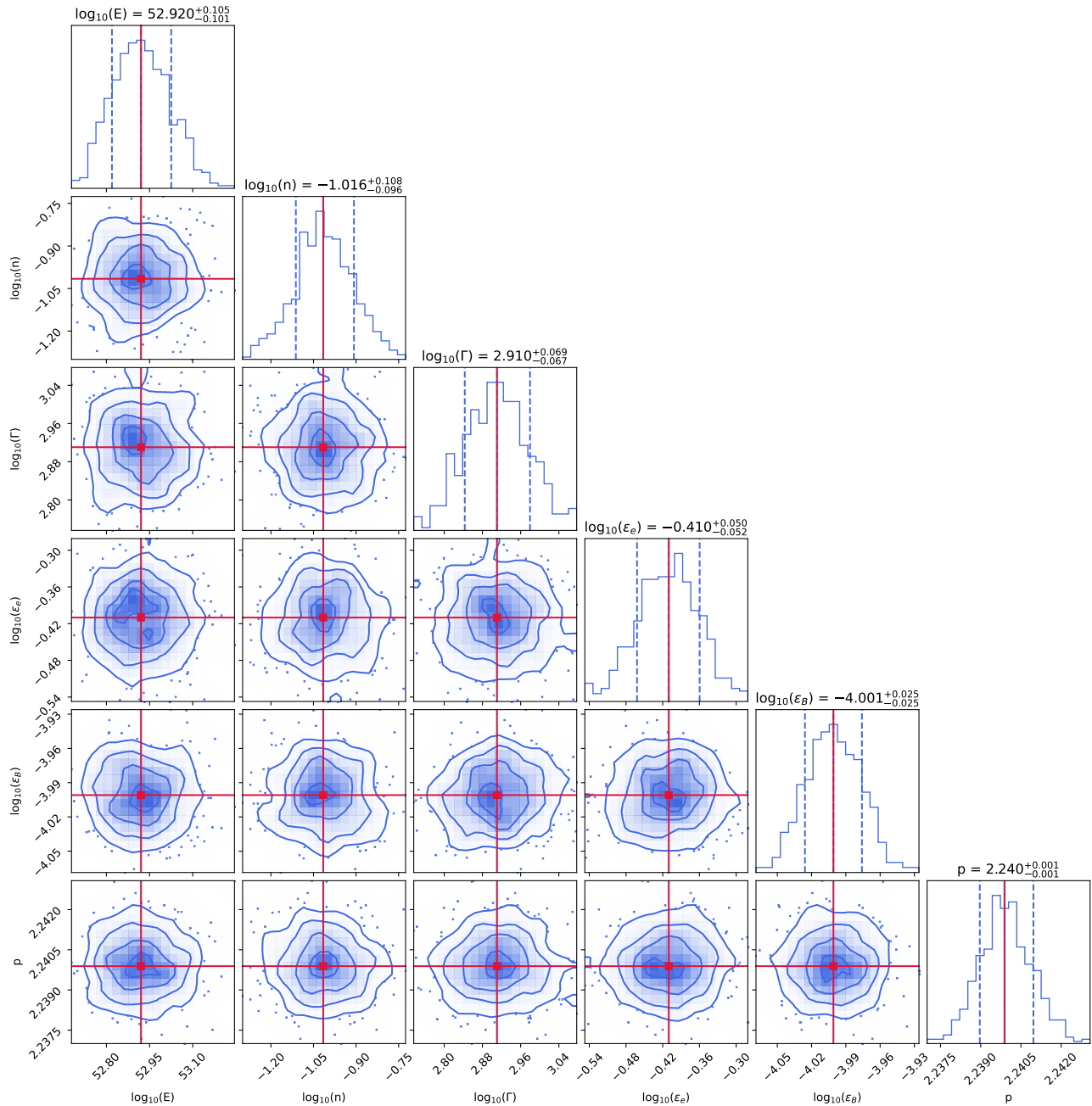


**Figure A6.** Corner plot of the parameters obtained from modelling the multiwavelength afterglow observations of GRB 080825C with the constant-density model shown in Section 2. The statistics for all parameters involved in the MCMC simulations are reported in Table A3.

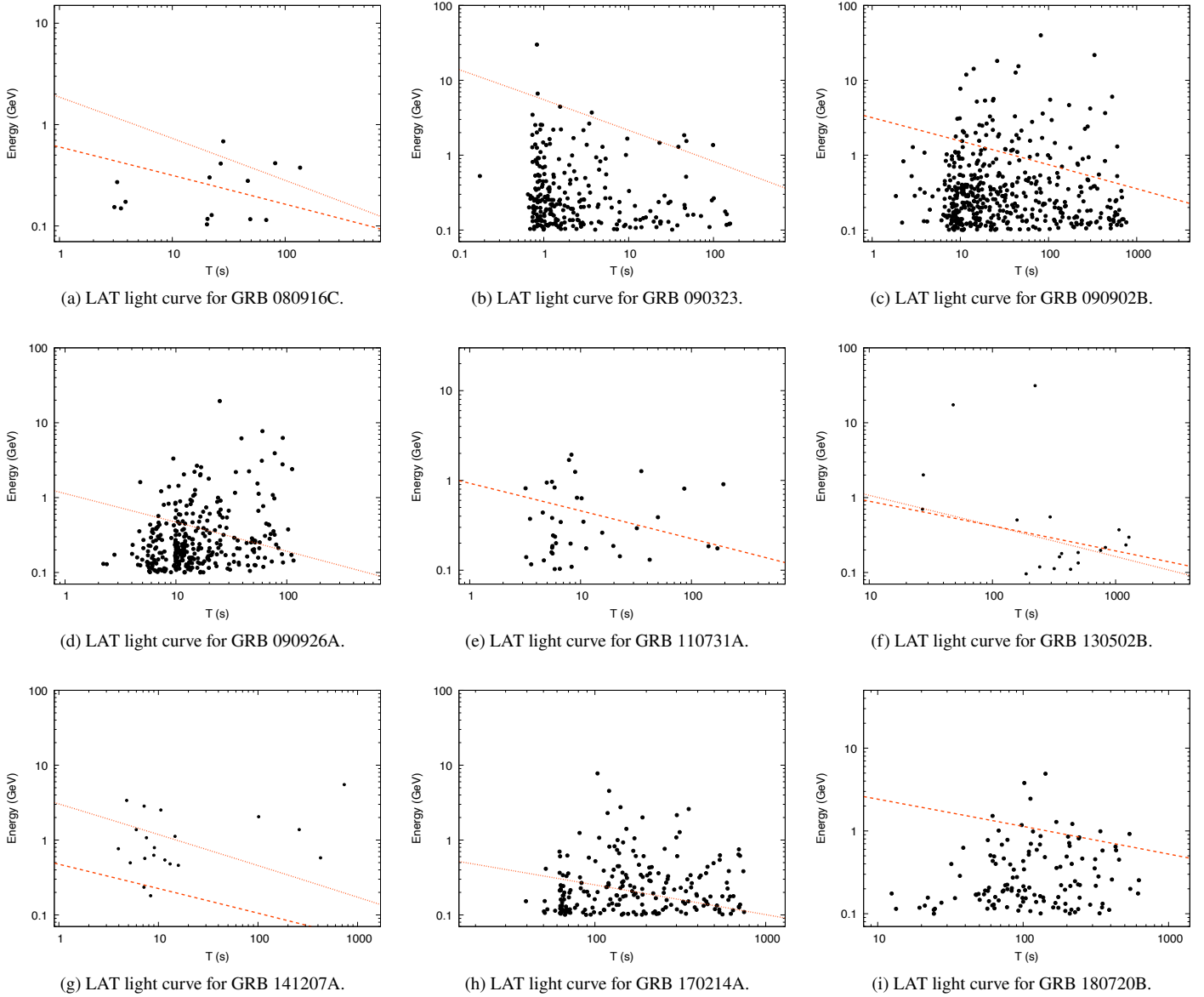


**Figure A7.** All the photons with energies  $> 100$  MeV and probabilities  $> 90\%$  of being associated with each burst in our sample. The red lines correspond to the maximum photon energies from our synchrotron afterglow model evolving in a constant-density (dotted) and stellar-wind (dashed) medium.